PAPER

Check for updates

Optimizing Cs$_2$CuBiBr$_6$ double halide perovskite for solar applications: the role of electron transport layers in SCAPS-1D simulations

Khandoker Isfaque Ferdous Utsho,[a] S. M. G. Mostafa,[a] Md. Tarekuzzaman, [iD] [ab] Muneera S. M. Al-Saleem,[c] Nazmul Islam Nahid,[ab] Jehan Y. Al-Humaidi, [iD] [c] Md. Rasheduzzaman,[ab] Mohammed M. Rahman [iD] *[d] and Md. Zahid Hasan [iD] *[ab]

Perovskite solar cells are commonly employed in photovoltaic systems because of their special characteristics. Perovskite solar cells remain efficient, but lead-based absorbers are dangerous, restricting their manufacture. Therefore, studies in the field of perovskite materials are now focusing on investigating lead-free perovskites. The SCAPS-1D simulator is used to simulate the impact of lead-free double perovskite as the absorber in perovskite solar cells. The research examines how the effectiveness of solar cells is impacted by a hole transport layer (CBTS) and several electron transports layers (WS$_2$, C$_{60}$, PCBM, and TiO$_2$), using Ni and Al acting as the back and front contacts metal. This work explores the impact of a Cs$_2$CuBiBr$_6$ perovskite as a solar cell absorber. The effectiveness of these device structures depends on defect density, absorber thickness, ETL thickness, and ETL combination. With WS$_2$, C$_{60}$, PCBM, and TiO$_2$, the device's power conversion efficiency (PCE) is 19.70%, 18.69%, 19.52%, and 19.65%, respectively. This research also highlights the impact of the absorber and HTL thickness. This investigation further included the analysis of the valence band offset (VBO) and conduction band offset (CBO). We also investigated the current density–voltage (*J–V*), quantum efficiency (QE), series and shunt resistance, capacitance-Mott–Schottky characteristics, and photocarrier generation–recombination rates and effective temperature. This study provides crucial structural design guidelines for a lead-free double perovskite device and highlights solar energy optoelectronic developments.

1. Introduction

With the potential to significantly influence human society and mold the future of renewable energy, solar cells represent a promising technological advancement. Sustainable energy is a plentiful resource that emits no carbon dioxide, is free to use, and is freely available.[1,2] Photovoltaic cells use visible light to generate power by converting solar photons to electric energy.[3,4] In the last two decades, significant technological advancements in photovoltaic technology have driven substantial cost reductions and remarkable improvements in the PCE of PV cells. The exploration and application of innovative materials present

exciting possibilities for even greater advancements in the years to come.[5,6] There are three generations of photovoltaic cell technology. In 1954, Bell Laboratories produced the first generation, with an efficiency of 6%. Second-generation solar cells, also called thin-film photovoltaic cells, offer a more affordable option than conventional silicon wafer-based cells. These thin-film cells have clear benefits in terms of material efficiency and lower total mass. They are distinguished by their flexibility and lightweight construction.[3,7] Third-generation solar cells have improved dependability and efficiency compared to previous versions. The exceptional efficiency of these cells is due to their diversified composition, particularly including conductive polymers, organic dyes, silicon nanowires, and nanomaterials with large band gaps.[8–10]

The SCAPS-1D simulator has been utilized by researchers for numerical simulations, utilizing computational analysis to support cost-effective production processes and optimize solar cell design. Before a device is put into production, it can be thoroughly evaluated in a virtual environment using simulation tools, which can save a lot of resources and time.[11] The SCAPS 1D simulation program facilitates the exploration and linkage of experimental as well as theoretical studies. Previously, planar FA-based PSCs were analyzed and their performance was

[a] Department of Electrical and Electronic Engineering, International Islamic University Chittagong, Kumira, Chittagong, 4318, Bangladesh. E-mail: zahidhasan.02@gmail.com

[b] Materials Research and Simulation Lab, Department of Electrical and Electronic Engineering, International Islamic University Chittagong, Kumira, Chittagong, 4318, Bangladesh

[c] Department of Chemistry, Science College, Princess Nourah bint Abdulrahman University, P.O. Box 84428, Riyadh 11671, Saudi Arabia

[d] Center of Excellence for Advanced Materials Research (CEAMR) & Chemistry Department, King Abdulaziz University, Jeddah 21589, Saudi Arabia. E-mail: mmrahman@kau.edu.sa

illustrated using both numerical simulations and experimental analysis.[12] More than ever, the necessity of alternative energy sources is highlighted by the world's expanding energy demand, the increasing exhaustion of fossil fuel resources, and the rising levels of pollution that feed global warming.[13–15] Renewable energy is becoming increasingly acknowledged as a vital source of electricity because of the worldwide problem of global warming. Especially remarkable is solar power, which is the most abundant energy resource on the planet. The high initial prices and low conversion efficiency of solar power generation remain barriers to mainstream adoption. It is anticipated that advancements in perovskite-based solar cell structure will increase production capacity while lowering resource and energy consumption.[16,17] The key factors driving perovskite film photovoltaics' growing popularity are their ability to produce them quickly and effectively, as well as the low material requirements and resulting cost reductions.[6,18–20]

The perovskite material, such as lead-free double perovskite structure $Cs_2B'B''Br_6$ where $B' = Cu$ and $B'' = Bi$. This perovskite structure is a lead-free non-toxic substance with preferred absorption.[21] Increased charge carrier production, a higher rate of photon generation, resulting in reduced energy loss and an enhanced concentration of electric charge carriers at the electrodes.[22,23] In comparison to conventional bismuth-based double perovskite solar cells, Cesium Copper Bismuth Bromide ($Cs_2CuBiBr_6$), referred to as the absorber, demonstrates enhanced thermal stability, owing to its single crystal structure and lower susceptibility to moisture. When compared to $CH_3NH_3PbX_3$, McClure and coworkers observed that $Cs_2AgBiBr_6$ and $Cs_2AgBiCl_6$ had a superior bandgap and good stability.[24] $Cs_2AgBiBr_6$ and $Cs_2AgBiCl_6$ exhibit poor efficiency due to high charge carrier effective masses, insufficient charge carrier transport properties, and large band gaps (>2 eV),[25–27] making them unsuitable for solar cell applications. Conversely, compared to $Cs_2AgBiBr_6$ and $Cs_2AgBiCl_6$, the $Cs_2CuBiBr_6$ absorber demonstrated an ideal band gap (1.24 eV), larger light absorption abilities, and superior performance, making it appropriate for the PSC.[21,28,29] Due to its substantial bandgap, which is closely correlated with V_{OC}, the inclusion of bromide in the perovskite might facilitate a high V_{OC}. In addition to the preferred optical band gap and light spectrum, their strength under illumination in humid conditions, and elevated temperatures are markedly enhanced in comparison to organic lead halide perovskites.[30] In PSCs, utilizing an appropriate electron transport layer (ETL) and a hole transport layer (HTL) can improve the absorber's performance and efficiency. A light-absorbing perovskite layer is often positioned between the ETL and the HTL in mesoporous and planar structures, which are common in solar cell systems. Electrons can move between mesoscopic perovskite structures and nanoparticles of mesoporous metal oxides like TiO_2 (ref. 31 and 32) and ZnO[33] through the ETL, while holes can successfully transmit through HTLs.[34] The thickness of the ETL, HTL, absorber layer, as well as their interface and phase matching characteristics, are the main determinants of photovoltaic parameters such as the open-circuit voltage (V_{OC}), short-circuit current density (J_{SC}), fill factor (FF), and power conversion efficiency (PCE). Several

semiconductor materials have been used as ETLs, including ZnO, TiO_2, WO_3, I_2O_3, WS_2, PCBM, C_{60}, Al_2O_3, and SnO_2.[35–38] Prior research has not extensively investigated the usage of ETLs like WS_2, PCBM, and CdS in combination with $Cs_2CuBiBr_6$ perovskite-based solar cells.[21] The ETL used in this work comprises Tungsten Disulfide (WS_2), Buckminsterfullerene (C_{60}), phenyl-C_{61} butyric acid methyl ester (PCBM), and Titanium Dioxide (TiO_2) as the electron transport materials. The electron transport layer made of tungsten disulfide (WS_2) is very desirable in optoelectronics because of its adaptability and excellent bandgap.[39,40] Furthermore, the effective extraction of electrons has been observed by organic electron transport layers, such as C_{60}, when combined with the perovskite layers.[41] The need for high-temperature heating of TiO_2 to attain the rutile form for solar application, along with the confined movement of electrons, impedes its effectiveness as an electron transport material in PSCs.[31,42–44] The PCBM ETL obviates the necessity for thermal annealing or processing at high temperatures, therefore considerably streamlining the production procedure and reducing production costs.

Moreover, the HTL and nearby surfaces affect the solar cell's efficiency, durability, and manufacturing cost.[45,46] Solar cell performance is improved by small-molecule HTLs; however, they don't have enough photostability and thermal stability. By comparison, polymeric HTLs are attractive because they are suitable with other materials, water-repellent, and can withstand high temperatures.[47] But these HTLs could have limitations with their optoelectronic characteristics, which might lead to lower efficiency. Due to the increasing demand for affordable solar cell manufacturing, earth-abundant, air-stable thin-film materials like copper barium thiocyanate (CBTS) are being investigated as possible substitutes for widely used HTLs like Cu_2O, CuSCN, $CuSbS_2$, NiO, P3HT, PEDOT: PSS, spiro-OMeTAD, CuI, CuO, and V_2O_5. CBTS is an appropriate option for HTL application due to its large atomic size, non-centrosymmetric crystal structure, high absorption coefficient, variable bandgap, and effective light-absorbing properties.[47–50] The shallow valence band of CBTS aligns well with $Cs_2B'B''Br_6$, leading to modest energy loss when CBTS is used as the hole transport layer in $Cs_2B'B''Br_6$ (where $B' = Cu$ and $B'' = Bi$) based PSCs. Prior research has shown that the CBTS HTL had favorable characteristics due to its suitable absorption coefficient and electron affinity.[51]

Therefore, ETL and HTL are implemented to improve the PV parameters of solar cells. Furthermore, this investigation on $Cs_2CuBiBr_6$ has shown substantial advancement, increasing efficiency from the previous 14.08% to an improved 19.70%. The energy band alignment was likely enhanced by the use of CBTS as a hole transport layer (HTL) and Ni as the back-contact metal, which decreased energy losses during charge carrier transport. This ideal alignment improves charge extraction and minimizes recombination. The use of ITO instead of FTO may have enhanced optical transmittance and electrical conductivity. Thus, more photons are able to reach the active perovskite layer, which improves the production of charge carriers. These results highlight the significant advancements attained in our study, which boost the performance of the examined absorber materials. Utilizing SCAPS-1D software to investigate single

absorber-based perovskite solar cells enhances experimental efficiency by virtually adjusting device settings. SCAPS-1D determines optimal designs and material selections by simulating many combinations, thus assisting experimentalists in the fabrication of high-performance devices.

This process expedites development, ensuring more efficient and accurate manufacturing procedures, eventually resulting in improved device performance. Therefore, this investigation entails the assessment of $Cs_2CuBiBr_6$ in a variety of configurations, such as WS_2, C_{60}, PCBM, and TiO_2 as electron transport layers (ETL), CBTS as hole transport layers (HTL), Al as the front contact metal, and Ni as the back-contact metal. The photovoltaic (PV) performance is investigated and evaluated by observing the impact of variations in the absorber thickness and ETL thickness, as well as the impact of series and shunt resistance on PV parameters, to determine the optimal configurations. To further understand the studied SC designs, we also compute the current–voltage (*J–V*) curves, capacitance–voltage (*C–V*) properties, quantum efficiency (QE), generation and recombination rate.

2. Device concept modeling and design

2.1. Numerical simulation employing SCAPS-1D

Understanding the basic principles of solar cells and determining the major variables affecting their efficiency is feasible through the computational model's framework. The SCAPS-1D application may be used to numerically solve significant 1D semiconductor problems.[52–55] Eqn (1) indicates that the charges are related to the electrostatic potential according to Poisson's equation.[56]

$$\frac{d^2}{dx^2}\psi = \frac{q}{\varepsilon_0\varepsilon_r}\left[p(x) - n(x) + N_d - N_A + \rho_p - \rho_n\right] \quad (1)$$

The above equation represents the electronic potential (ψ), relative permittivity (ε_r), free space permittivity (ε_0), ionized acceptor densities and donor densities (N_A and N_d), electron and hole densities (n and p), electron and hole distributions (ρ_p

and ρ_n), and electronic charge (q). When generation, recombination, drift, and diffusion are all evaluated at the same time, the continuity equation emerges as the governing equation. The continuity equations for the variation in electron and hole concentrations are presented in eqn (2) and (3).

$$\frac{\partial n}{\partial t} = \frac{1}{q}\frac{\partial J_n}{\partial x} + (G_n - R_n) \quad (2)$$

$$\frac{\partial p}{\partial t} = \frac{1}{q}\frac{\partial J_P}{\partial x} + (G_P - R_P) \quad (3)$$

In this scenario, J_n and J_P represent the current densities of electrons and holes, G_n and G_P represent electron and hole generation, and R_n and R_P represent electron and hole recombination. The charge carrier drift-diffusion equations used to compute the electron and hole current densities in solar cells are given by eqn (4) and (5).

$$J_n = q\mu_n n\varepsilon + qD_n\partial n \quad (4)$$

$$J_P = q\mu_P p\varepsilon + qD_P\partial p \quad (5)$$

Here, carrier mobility is indicated by μ_n and μ_P, whereas electron and hole diffusion coefficients are indicated by D_n and D_P. The coefficient of diffusion is dependent on the mobility and durability of the carrier, based on the Einstein relationship.[57] The film absorption constant was obtained using the newly modified E_g-sqrt model, an updated version of the conventional sqrt ($h\nu - E_g$) model. The "Tauc law" define this relationship as seen in eqn (6).

$$\alpha(h\nu) = \left(\alpha_0 + \beta_0\frac{E_g}{h\nu}\right)\sqrt{\frac{h\nu}{E_g} - 1} \quad (6)$$

where $h\nu$ denotes photon energy, bandgap, and absorption coefficient are represented by E_g. Eqn (7) and (8) establish a relationship between the model constants α_0 and β_0 and the standard model constants A and B, as shown below:
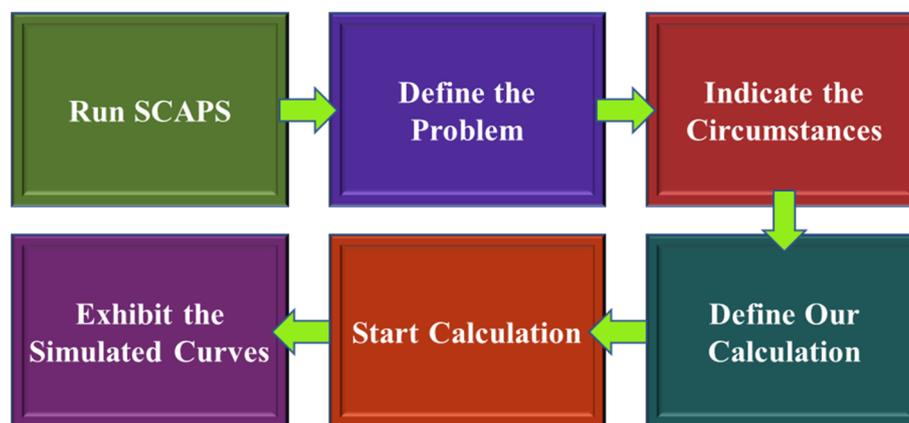
$$\alpha_0 = A\sqrt{E_g} \quad (7)$$

Fig. 1 SCAPS-1D operational instruction.

$$\beta_0 = \frac{B}{\sqrt{E_g}} \qquad (8)$$

Under steady-state factors, SCAPS-1D determines the basis of semiconductor equations. Fig. 1 describes the simulation technique of SCAPS-1D. The program was started to execute the SCAPS-1D simulation, and the solar cell's construction consisted of several layers such as WS_2, C_{60}, PCBM, and TiO_2 acting as ETL and $Cs_2CuBiBr_6$ acting as the absorber of perovskite. Inputs included material properties such as electron affinity, dielectric constant, carrier mobilities, bandgap, *etc.*, and operating characteristics such as temperature, AM1.5 G illumination intensity, bias voltage range for *J–V* characteristics, *etc.*

Capacitance, quantum efficiency (QE), *J–V* properties, Mott–Schottky characteristics were among the several measures that were considered. Next, we solved Poisson's equation, continuity equations, and drift-diffusion equations before initiating the simulation. We examined the results using graphical tools, such as origin, to evaluate the efficiency of solar cells.

2.2. Device structure

The main device's conceptual design is shown in Fig. 2a. The formation of the configuration of a lead-free double perovskite halide solar cell is accomplished by the combination of ETL, HTL, and back contact with the $Cs_2CuBiBr_6$ absorber layer. As a solar cell, the $Cs_2CuBiBr_6$ absorber has an n–i–p
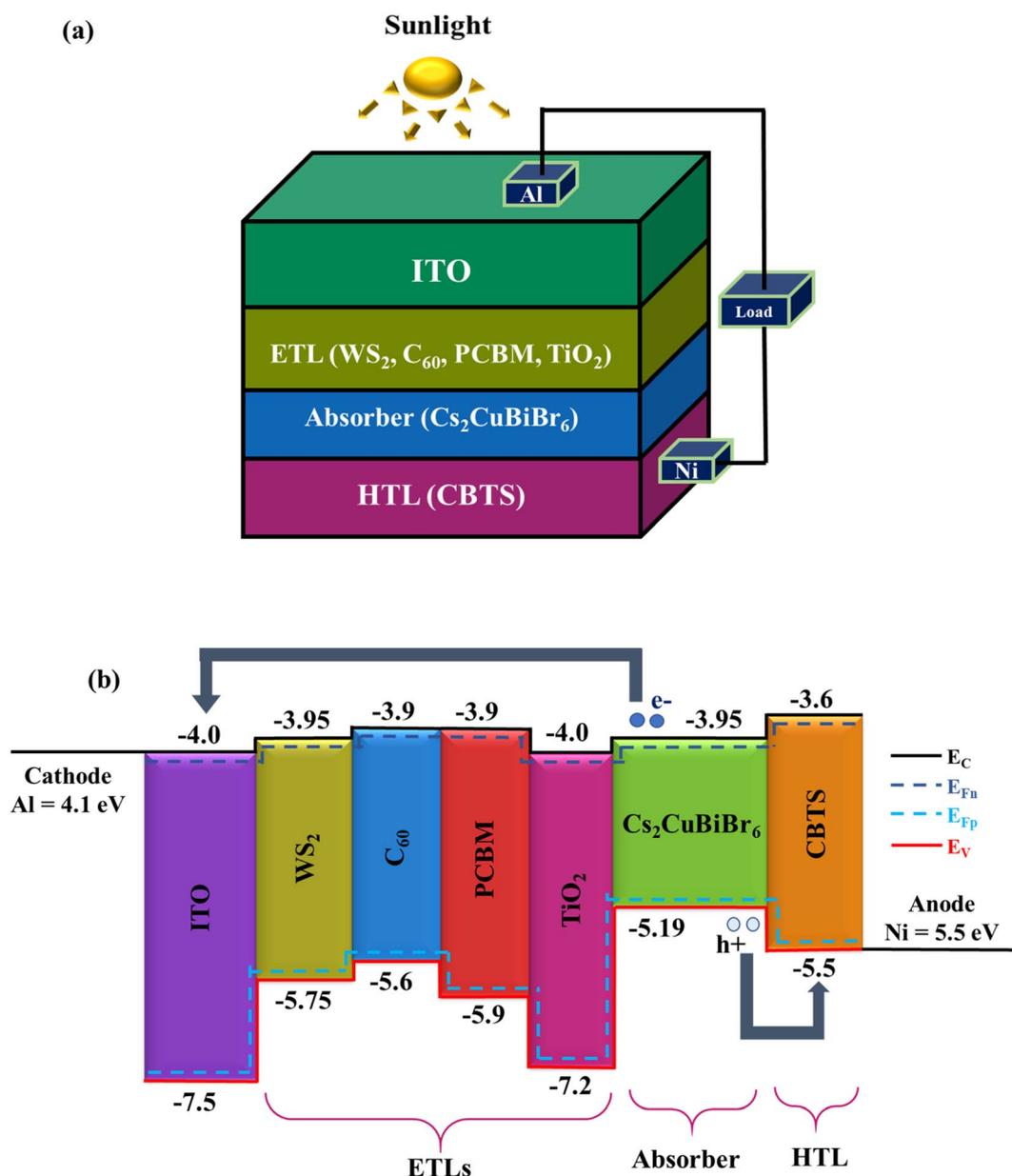

Fig. 2 The $Cs_2CuBiBr_6$ absorber's (a) crystal arrangement and (b) energy band aligning associated with various ETL materials (WS_2, C_{60}, PCBM, and TiO_2).

Table 1 Parameters applied in this research involve the absorber layer, HTL, ETL, and ITO

Parameter (unit)	ITO	ETL				Cs$_2$CuBiBr$_6$	HTL
		WS$_2$	C$_{60}$	PCBM	TiO$_2$		CBTS
Ref.	51 and 58	21 and 51	51 and 59	21 and 59	51 and 60	21	48 and 51
Thickness [μm]	0.5	0.1	0.05	0.05	0.03	0.6	0.100
Bandgap, E_g [eV]	3.5	1.8	1.7	2	3.2	1.24	1.90
Electron affinity, X [eV]	4	3.95	3.9	3.9	4	3.95	3.60
Dielectric permittivity, ε_r (relative)	9	13.6	4.2	3.9	9	5.40	5.40
CB effective density of states, N_C [cm^{-3}]	2.2×10^{18}	1×10^{18}	8.0×10^{19}	2.5×10^{21}	2×10^{18}	1.46×10^{19}	2.2×10^{18}
VB effective density of states N_V [cm^{-3}]	1.8×10^{19}	2.4×10^{19}	8.0×10^{19}	2.5×10^{21}	1.8×10^{19}	3.34×10^{19}	1.8×10^{19}
Electron thermal velocity [cm^{-1} s]	1×10^7	1×10^7	1×10^7	1×10^7	1×10^7	1.39×10^7	1×10^7
Hole thermal velocity [cm^{-1} s]	1×10^7	1×10^7	1×10^7	1×10^7	1×10^7	1.06×10^7	1×10^7
Electron mobility, μ_n [cm^2 V^{-1} s^{-1}]	20	100	8.0×10^{-2}	0.2	20	13.98	30
Hole mobility, μ_h [cm^2 V^{-1} s^{-1}]	10	100	3.5×10^{-3}	0.2	10	2.98	10
Shallow uniform donor density, N_D [cm^{-3}]	1×10^{21}	1×10^{18}	1×10^{17}	2.93×10^{17}	9×10^{16}	1×10^{15}	0
Shallow uniform acceptor density, N_A [cm^{-3}]	0	0	0	0	0	1×10^{15}	1×10^{18}
Defect density, N_t [cm^{-3}]	1×10^{15a}	1×10^{15}	1×10^{15}	1×10^{15}	1×10^{15}	1×10^{15a}	1×10^{15}
Capture cross-section for electrons [cm^2]	1×10^{-15}	1×10^{-15}	1×10^{-15}	1×10^{-15}	1×10^{-15}	1×10^{-15}	1×10^{-15}
Capture cross-section for holes [cm^2]	1×10^{-15}	1×10^{-15}	1×10^{-15}	1×10^{-15}	1×10^{-15}	1×10^{-15}	1×10^{-15}

Table 2 This perovskite solar cell for Cs$_2$CuBiBr$_6$ uses interface parameters

Interface	Defect type	Capture cross-section: electrons/holes [cm^2]	Distribution of energy	Reference for defect energy levels, E_t	Interface defect density [cm^{-2}]
ETL/Cs$_2$CuBiBr$_6$	Neutral	1×10^{-17} 1×10^{-18}	Single	Above the VB maximum	1×10^{10}
Cs$_2$CuBiBr$_6$/CBTS	Neutral	1×10^{-18} 1×10^{-19}	Single	Above the VB maximum	1×10^{10}

configuration. In this case, an n–i–p structure outperforms a standard semiconductor p–n junction due to its superior long-wavelength sensitivity. The depletion zone of an n–i–p structure is positioned deep inside the device, including the intrinsic area. Photons penetrate deeply into cells when they are subjected to long wavelengths. Despite this, the creation of electron–hole pairs within and outside the zone of depletion is the only source of current. An increase in depletion width allows for more effective production and distinction of electron–hole pairs, which ultimately turn increases the cell's quantum efficiency.[51] The photon-capturing properties of Cs$_2$CuBiBr$_6$ are a result of its double heterostructure, which guarantees charge and photon confinement and functions as an ohmic contact around the heavily doped ETL and HTL. When designing this device, we keep the following elements in consideration: CBTS for the HTL, Ni for the back-metal contact, Al for the front-metal contact, WS$_2$, C$_{60}$, PCBM, and TiO$_2$ for the ETLs, and cesium copper bismuth bromide for the absorber layer. Fig. 2a depicts the structure of the ITO/ETL/Cs$_2$CuBiBr$_6$/CBTS/Ni device. The simulated input parameters for the absorber layer, ETLs, along with HTL, are presented in Table 1, along with the input parameters for the interfacial defect layers included in Table 2. While we execute the SCAPS-1D investigation, the software helps us analyze the performance of different double PSC configurations. The formation of double perovskite structures is achieved by maintaining an ambient temperature of 300 K, a frequency of 1 MHz, and an AM1.5G spectrum.

2.3. Band orientation of Cs$_2$CuBiBr$_6$ utilizing absorber with various ETLs

The band orientation of several heterostructures based on the Cs$_2$CuBiBr$_6$ absorber is shown in Fig. 2b. It shows the valence band maxima (E_V), conduction band minima (E_C), and the quasi-Fermi levels of electrons (F_n) and holes (F_p). While F_n and E_C continue to exhibit a harmonic connection, F_p aligns with E_V in different kinds of ETL. F_n and E_V stay at equal levels across all ETLs using CBTS as the HTL; therefore, F_n intersects E_C and inhibits the flow of holes and electrons from ETLs and HTL. A nickel (Ni) back contact with a work function (WF) of 5.5 eV effectively captures holes from the HTL, while aluminum (Al) front contact, having a work function (WF) of 4.1 eV efficiently collects electrons.

3. Result and discussion

3.1. Impacts of conduction band offset (CBO) and valence band offset (VBO)

The ETL and HTL are required for efficiently moving photo-generated charge carriers from the absorber to their specific contacts in perovskite solar cells. Furthermore, they restrict the recombination of charges at the ETL/absorber and absorber/HTL interfaces by delaying the movement of electrons and holes toward specific charge carrier accumulation at each electrode.[61] When sunlight strikes the solar cell, the perovskite absorber produces electrons and holes.

Subsequently, these charge carriers are split up and distributed to the relevant contacts for collection. The effectiveness of the splitting process depends on the conduction band offset (CBO) and valence band offset (VBO) at the ETL/absorber and absorber/HTL interfaces, respectively. The performance of the device is directly affected by these offsets. At the ETL/absorber interface and absorber/HTL interface, there are three distinct kinds of barriers: cliff-like, nearly flat, and spike-like.[62] The energy differential in cliff-like barrier facilitates the movement of carriers, owing to the band bending at the interfacial layers. In particular, when interface defects are present, band bending in a cliff-like barrier accelerates recombination at the interface, which reduces the V_{OC} and lowers the solar cell's efficiency. The energy difference is zero, and there is no band offset in a nearly flat barrier. Here, the interfaces of CBO and VBO are almost flat, and the produced electrons and holes may move freely due to the absence of an energy barrier. When the spike-like barrier is present, the energy differential, caused by the shape of band bending at the layer interface, prevents transporting carriers from moving through the structure. Spike-like band bending reduces recombination at the interface, especially between absorber valence band holes (conduction band electrons) and ETL conduction band electrons (HTL valence band holes).[63–66]

The CBO at the ETL/absorber interface is defined as

$$CBO = X_{absorber} - X_{ETL} \qquad (9)$$

While X_{ETL} exceeds $X_{absorber}$, a negative CBO for a cliff-like barrier indicates that the ETL's conduction band minimum (CBM) is smaller compared to the absorber's. If the value of CBO is zero, then the barrier is nearly flat. Conversely, the barrier of spike-like, having a positive CBO, is seen when the CBM of the ETL is greater than the CBM of the absorber ($X_{ETL} < X_{absorber}$).

Conversely, the VBO at the absorber/HTL interface is defined as[61]

$$VBO = X_{HTL} - X_{absorber} + E_{g,HTL} - E_{g,absorber} \qquad (10)$$

VBO is depicted as Valence Band Offsets, X_{HTL} represents the electron affinity of the HTL, while $E_{g,absorber}$ and $E_{g,HTL}$ denote the bandgaps of the absorber and HTL, consequently.

The absorber/HTL interface and the ETL/absorber interface both exhibit similar barrier types. The absorber exhibits a cliff-like barrier having a negative VBO when its valence band maximum is less than the HTL's. When the VBO is zero and the barrier is nearly flat, there is no band offset. On the other hand, the barrier of spike-like occurs when the HTL's valence band maximum is less than the absorber's and may be identified by a positive VBO.

Eqn (9) and (10) were used to determine the CBO and VBO.[61] For WS$_2$ the conduction band offset (CBO) and valence band offset (VBO) are given below.

The CBO at the interface between the absorber and ETL is = $X_{absorber} - X_{ETL} = 3.95 - 3.95 = 0$ eV.

This indicates that the CBO is at zero, and the barrier is nearly flat.

Table 3 Determined the value of VBO and CBO utilizing various ETLs

Absorber	ETLs	CBO	VBO
Cs$_2$CuBiBr$_6$	WS$_2$	0	0.31
	C$_{60}$	0.05	0.31
	PCBM	0.05	0.31
	TiO$_2$	−0.05	0.31

The VBO at the HTL and the absorber interface is = $X_{HTL} - X_{absorber} + E_{g,HTL} - E_{g,absorber} = 3.6 - 3.95 + 1.9 - 1.24 = 0.31$ eV.

The calculation shows that the VBO is positive, and the barrier is spike-like.

The values of CBO and VBO were determined using the same approach as for the remaining ETLs in Table 3. For the ETL C$_{60}$, both the CBO and VBO exhibit positive values, forming spike-like barriers. Similarly, in the case of the ETL PCBM, both CBO and VBO are positive and also form spike-like barriers. In contrast, the ETL TiO$_2$ presents a negative CBO, forming a cliff-like barrier, while the VBO remains positive, forming a spike-like barrier.

The higher V_{OC} in the CBTS device, featuring a spike-like barrier, is attributed to reduced recombination at the absorber/CBTS interface, thereby enhancing carrier collecting efficiency. Conversely, the cliff-like barrier in the spiro-OMeTAD device enhances hole transport but results in increased recombination, hence reducing V_{OC}.[21] Therefore, despite the less effective hole transport, the spike-like barrier in CBTS reduces recombination, leading to a higher V_{OC} and overall superior device performance.

3.2. Band diagram

With the use of cesium copper bismuth bromide, the energy band diagrams of the PSCs that were utilized are shown in Fig. 3a–d. The offset between the valence and conduction bands, that indicates disparity in the valence band between the HTL and absorber layer, is affected through every ETL in this scenario, including an absorbing layer of Cs$_2$CuBiBr$_6$ as well as CBTS considering the HTL. The PSC's reliability and efficacy are highly influenced by the energy level alignment. In PSCs, photogenerated electrons are injected into the ETL's conduction band while holes are simultaneously transported to the HTL. The next step is collecting the electrons and holes from the front-contact metal (Al) and the back-contact metal (Ni), according to the sequence. If the energy levels (conduction band and valence band) of the materials interacting at an interface are not perfectly matched, a phenomenon known as energy band mismatch will occur. The device's performance characteristics have a major impact on the energy band mismatch at the Cs$_2$CuBiBr$_6$ and HTL as well as ETL and Cs$_2$CuBiBr$_6$ interfaces. To enable effective electron extraction, the ETL's conduction band minimum (CBM) should be either slightly lower than or closely aligned with the CBM of Cs$_2$CuBiBr$_6$. Likewise, to facilitate efficient hole transmission, the valence band maximum (VBM) of the HTL should be in near alignment with or somewhat higher than the VBM of Cs$_2$CuBiBr$_6$. Any large mismatch may result in energy barriers that reduce carrier transit and increase

interfacial recombination, both of which reduce the efficiency of the device. Consequently, electronic property tuning of ETL and HTL materials becomes an essential task. To properly remove electrons at the interface ETL/$Cs_2CuBiBr_6$, the electron affinity of ETL should be greater than that of $Cs_2CuBiBr_6$. On the other hand, the HTL must have a lower ionization energy to extract holes at the interface $Cs_2CuBiBr_6$/HTL. Fig. 3 shows that in the four best configurations of $Cs_2CuBiBr_6$-based devices, the Fermi level moves inside the conduction band, which is close to it. In the $Cs_2CuBiBr_6$-based device, the Fermi level crossed the conduction band with WS_2 as the layer of ETL and CBTS as the layer of HTL (Fig. 3a). Fig. 3b–d illustrate the various architectures of devices based on $Cs_2CuBiBr_6$ perovskite. The degenerate semiconductor nature and pattern of C_{60}, PCBM, and TiO_2 as ETL and CBTS as HTL were similar to those illustrated in Fig. 3a. All four ETLs (WS_2, C_{60}, PCBM, TiO_2) provide identical results when used with the same heterostructure; this is because their bandgap energies are 1.8, 1.7, 2, and 3.2 eV, respectively. The energy of the valence band is almost equal to that of the quasi-Fermi levels F_n and F_p, as seen in Fig. 3a–d. F_p is always higher than E_V and F_n, and the conduction band (E_C) also shows synchronized behavior.

3.3. Variation of absorber layer thickness and ETL layer thickness on PV performance for $Cs_2CuBiBr_6$

The ETL, positioned between the ITO and the absorber layer, may extremely influence the absorber layer's interaction with photons. To improve the PV output properties of the SCs, the thickness of the layer covering the absorber and the ETL is essential. The best-performing solar collectors need PV output tuning.[67] For this study, we considered WS_2, C_{60}, PCBM, and TiO_2 to be ETL, $Cs_2CuBiBr_6$ to be an absorber, and CBTS to be HTL. Fig. 4–7 show the contour maps of V_{OC}, J_{SC}, FF, and PCE for $Cs_2CuBiBr_6$ absorber-based PSCs, with performance varying with absorber thickness (0.4–1.2 μm) and ETL thickness (0.03–0.15 μm).

Fig. 4a illustrates that the maximum V_{OC} levels were observed when the absorber layer thickness was adjusted from 0.4 to 0.45 μm, while the thickness of ETL ranged from 0.03 to 0.15 μm. When the ETL layer thickness increases, the absorber layer thickness remains constant, but V_{OC} may decrease if the absorber layer is increased (Fig. 4a). The thickness of absorber layer remains constant for the C_{60}, PCBM, and TiO_2 structures, regardless of the increase in the ETL layer thickness (Fig. 4b–d).
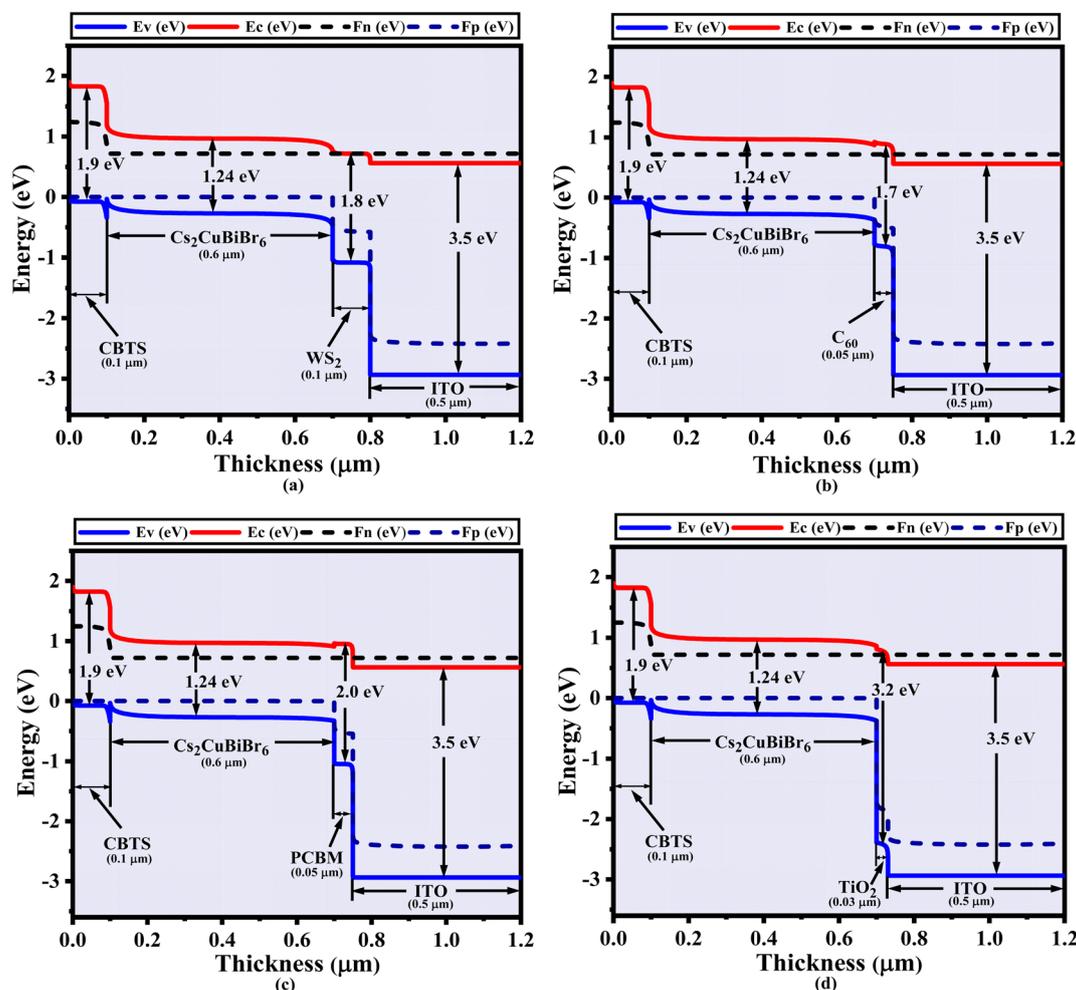

Fig. 3 Band diagram containing (a) WS_2, (b) C_{60}, (c) PCBM, and (d) TiO_2 for $Cs_2CuBiBr_6$.
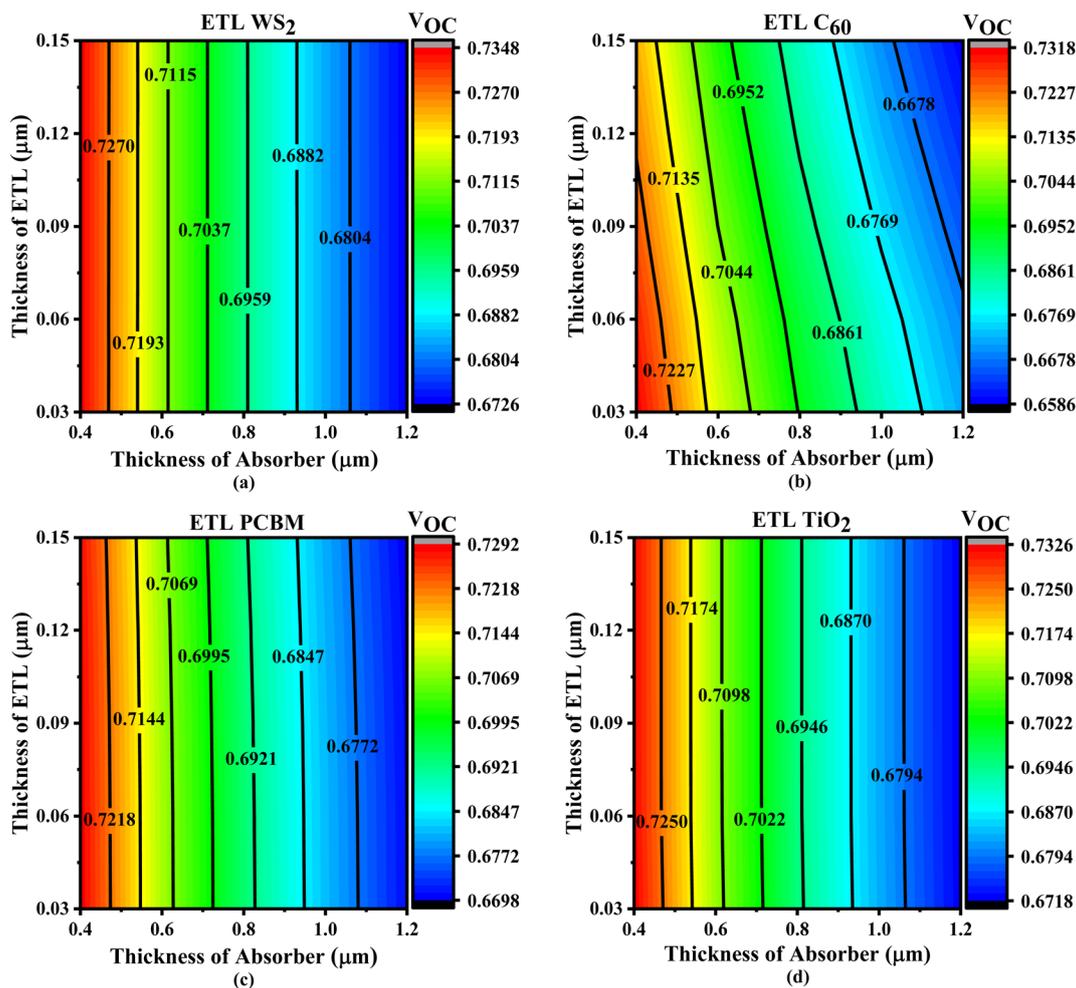
Fig. 4 Contour plots of V_{OC} resulting from the sequential change in absorber layer thickness and ETL layer thickness with ETLs including (a) WS$_2$, (b) C$_{60}$, (c) PCBM, and (d) TiO$_2$.

No matter how thick the ETL is, the WS$_2$, PCBM, and TiO$_2$ structures attained the greatest value of V_{OC} values considering the thickness of absorber layers are about 0.4 μm and 0.045 μm thick, respectively (Fig. 4a, c and d). Regarding the C$_{60}$ ETL-based structure, the maximum V_{OC} is found while the thickness of absorber is generally 0.4 to 0.45 μm and the thickness of the ETL is around 0.07 μm (Fig. 4b). Overall, most of the solar systems that were considered might have fewer V_{OC} with increasing absorber layer, as shown in Fig. 4. An increase in saturation current exceeding the photocurrent in the presence of a thick absorber layer can explain this phenomenon by increasing the carrier recombination rate.[68]

In Fig. 5, we observe how the J_{SC} parameters of four different perovskite solar cells are affected by using different ETL and absorber layer thicknesses. The maximum J_{SC} values (36.77–37.24 mA cm^{-2}) for WS$_2$-based solar cells are noted when the thickness of absorber is between 0.89 and 1.2 μm and the thickness of ETL is between 0.03 and 0.15 μm (Fig. 5a). Based on absorber thicknesses of 0.89–1.2 μm, the PCBM and TiO$_2$ ETL-based solar cells exhibit the same pattern, with peak J_{SC} values of 36.77–37.25 mA cm^{-2} and 36.77–37.26 mA cm^{-2},

respectively (Fig. 5c and d). Increasing the absorber thickness while maintaining the ETL thickness results in higher J_{SC} values. If the absorber layer is thicker, higher light absorption, providing a higher generation rate and J_{SC} values. To minimize the effects of series resistance, thinner ETL layers may raise the current by decreasing the amount of recombination between electron–hole pairs. Keeping the ETL thickness at a minimum is recommended to enhance J_{SC}, V_{OC}, and overall efficiency. This will help minimize the production of large pinholes and rough surfaces. For WS$_2$, PCBM, and TiO$_2$ ETL-based solar cells, the appropriate absorber thickness is usually determined to be between 0.89 and 1.2 μm, and the ETL thickness does not affect J_{SC} fluctuation (Fig. 5a, c and d). Finally, Fig. 5b shows that the C$_{60}$-based ETL solar cells have the greater J_{SC} value (35.61–36.85 mA cm^{-2}) when the absorber thickness is between 0.68 and 1.2 μm and the ETL thickness is between 0.03 and 0.05 μm. The observation shows that a smaller ETL and a thicker absorber may result in a higher J_{SC} for C$_{60}$. Increasing the generation rate and greater J_{SC} is possible with a larger absorber layer since it improves light absorption.[68] The impact of series resistance may be alleviated by a thin electron transport layer (ETL), which
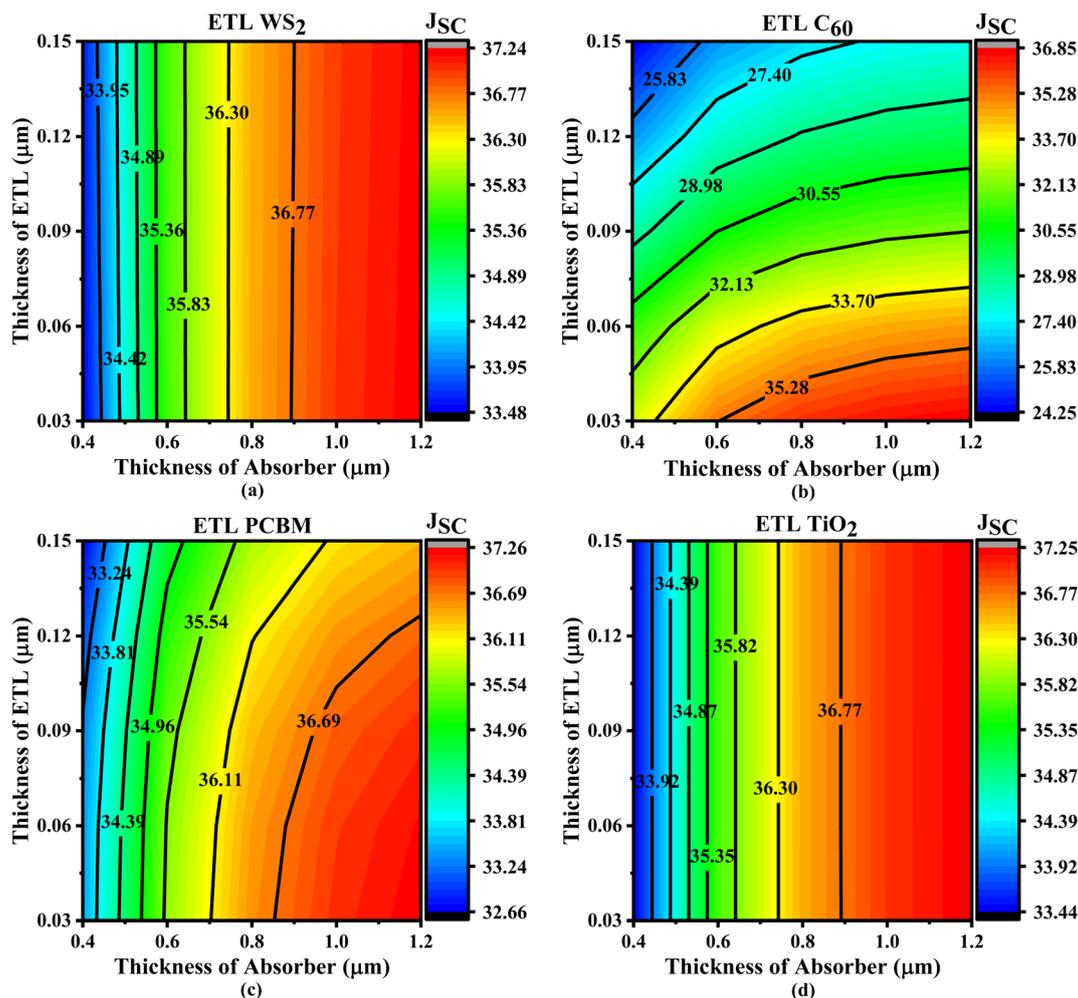
Fig. 5 Contour plots of J_{SC} resulting from the sequential change in absorber layer thickness and ETL layer thickness with ETLs including (a) WS$_2$, (b) C$_{60}$, (c) PCBM, and (d) TiO$_2$.

enhances current by diminishing the chance of recombination of electron–hole pairs. Crucially for J_{SC}, reducing the ETL thickness mitigates the development of bigger pinhole and uneven surface.[68]

Fig. 6 depicts the change of the fill factor (FF) for perovskite solar cells following variations in the absorber and ETL thickness. For Cs$_2$CuBiBr$_6$-based PSCs, the WS$_2$ ETL had an FF of 78.98% when the thickness of absorber layer was between 0.4 and 0.5 µm and the ETL thickness was between 0.03 and 0.15 µm, shown in Fig. 6a. When the thickness of absorber varies from 0.4 to 0.5 µm and the thickness of ETL varies from 0.03 to 0.15 µm, the FF value is observed in solar cells connected to ETLs C$_{60}$, PCBM, and TiO$_2$-related solar cells, as shown in Fig. 6b–d. This pattern is almost identical to the one that we have found. With the increase in thickness of the absorber layer, the value of FF decreases, and it is not affected by the change in the thickness of the ETL. Alteration to the ETL's thickness may lead to a relationship between rising series resistance and falling FF with increasing absorber thickness.[69]

Fig. 7 depicts contour plots that demonstrate changes in PCE for different solar structures when the thickness of the absorber

and ETL layers is changed. The ETL WS$_2$ solar design attained optimal efficiency of 19.71% within the absorber thickness range of 0.50 to 0.65 µm and the ETL thickness range of 0.03 to 0.15 µm shown in Fig. 7a. When the absorber thickness varied from 0.5 to 0.65 µm and the ETL thickness varied from 0.03 to 0.15 µm, the devices that employed TiO$_2$ ETL also demonstrated an excellent PCE of 19.65%, illustrated in Fig. 7d. According to Fig. 7c, the PCBM ETL also demonstrated consistent PCEs of 19.55%, with an absorber thickness ranging from 0.55 to 0.65 µm and an ETL thickness ranging from 0.03 to 0.085 µm. In contrast to alternative devices, the PSC with C$_{60}$ ETL demonstrated the lowest PCE of 19.42%, with an absorber thickness between 0.43 to 0.75 µm and an ETL thickness of around 0.03 µm, as seen in Fig. 7b.

3.4. Variation of absorber layer thickness and defect density on PV performance for Cs$_2$CuBiBr$_6$

Since there is a direct relationship between defect density (N_t) and the absorber layer thickness, the entire thickness of the absorber layer has a major impact on the efficient operation of
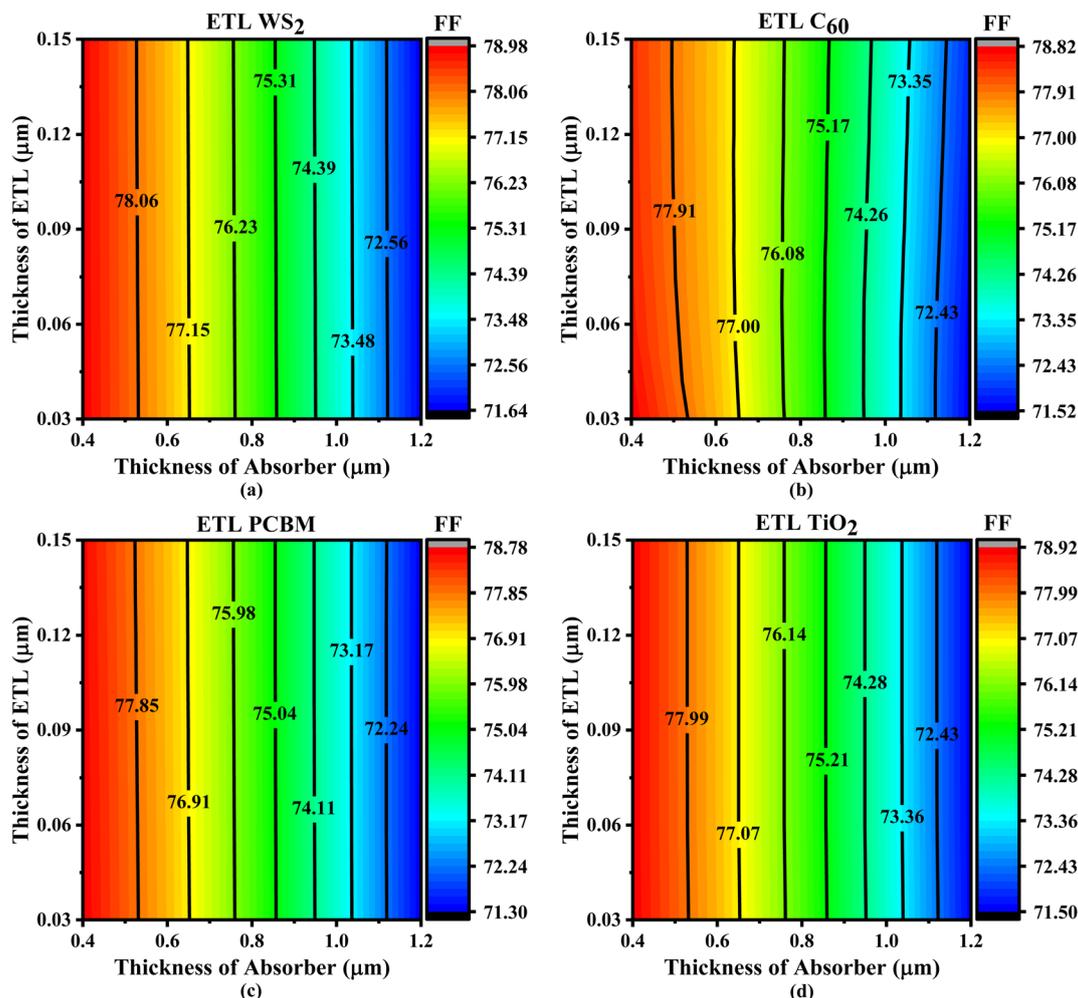
Fig. 6 Contour plots of FF resulting from the sequential change in absorber layer thickness and ETL layer thickness with ETLs including (a) WS_2, (b) C_{60}, (c) PCBM, and (d) TiO_2.

solar cells (SC_S) and photovoltaic (PV) devices.[68] A decrease in stability and PCE occurs in PSC_S as a result of film disintegration with the creation of pinholes caused by an increase within the defect density (N_t) in the absorber layer.[70] This section explores the overall effect of defect density (N_t) and absorber thickness on a photovoltaic cell that is based on a $Cs_2CuBiBr_6$ absorber. Fig. 8–11 shows the results of the simulations that analyzed the effect of different absorber thicknesses ($0.4-1.2$ μm) and N_t values ($1 \times 10^{15} - 1 \times 10^{19}$ cm^{-3}) on the PV performance characteristics of the four optimal PSCs.

Fig. 8 illustrates the impact contour plot visualization on the V_{OC} parameter for properties being examined. This visualization was applied to sequentially change the thickness of the absorber layer and N_t. When absorber thickness varies between $0.4-0.8$ μm and N_t varies between $1 \times 10^{15} - 1 \times 10^{17}$ cm^{-3}, the highest V_{OC} that can be produced using WS_2-based ETLs is 0.7360 V, as shown in Fig. 8a. The V_{OC} for TiO_2 ETL-related PSC is 0.7340 V when the absorber thickness is between $0.4-0.8$ μm and N_t is between $1 \times 10^{15} - 1 \times 10^{17}$ cm^{-3}, depicts in Fig. 8d. A constant V_{OC} of 0.7320 V was also demonstrated by the C_{60} ETL, with absorber thicknesses ranging from $0.4-0.8$ μm and N_t

ranging from $1 \times 10^{15} - 1 \times 10^{17}$ cm^{-3}, illustrated in Fig. 8b. Compared to other devices, the PSC with PCBM ETL exhibited the lowest V_{OC} of 0.730 V, with an absorber thickness varying between $0.4-0.8$ μm and N_t between $1 \times 10^{15} - 1 \times 10^{17}$ cm^{-3}, as seen in Fig. 8c. It was noted that when absorber thickness was varied with defect densities for WS_2, C_{60}, PCBM, and TiO_2, a similar impact was seen with ETL-based SC configurations.

The effect of changing absorber thickness and defect density on J_{SC} is demonstrated in Fig. 9a, c and d. When the absorber thickness is between $0.7-1.2$ μm and N_t fluctuates between $1 \times 10^{15} - 1 \times 10^{17}$ cm^{-3}, the J_{SC} for WS_2, PCBM, and TiO_2 ETLs achieves 37.30 mA cm^{-2}. In contrast, at the same thickness of the absorber and N_t ranges, the C_{60}-based optimal device attains a J_{SC} value of 35.70 mA cm^{-2}, illustrated in Fig. 9b. Therefore, as the absorber thickness and defect density increase, the J_{SC} value also increases.

Regarding all four structures under consideration, Fig. 10 depicts the impact of varying N_t and absorber layer thickness on FF. When the absorber thickness is between $0.4-0.8$ μm and the N_t falls within the range of $1 \times 10^{15} - 1 \times 10^{17}$ cm^{-3}, the WS_2-based PSC achieves the highest FF of 79.00%, shown in Fig. 10a.
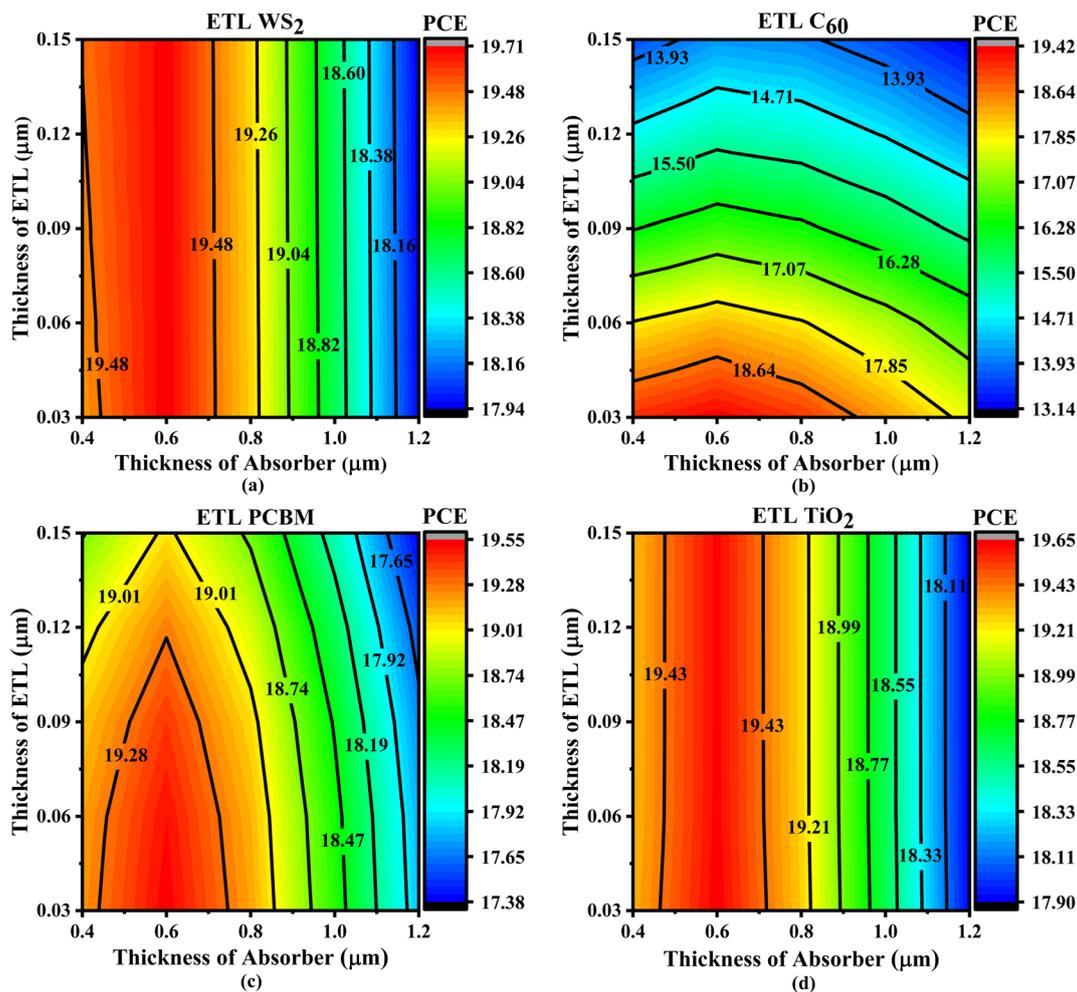
Fig. 7 Contour plots of PCE resulting from the sequential change in absorber layer thickness and ETL layer thickness with ETLs including (a) WS_2, (b) C_{60}, (c) PCBM, and (d) TiO_2.

The result for TiO_2 is also similar, according to Fig. 10d. Conversely, the solar cell design based on ETL, C_{60} shows smaller FF values, measuring 78.80% in cases when the absorber thickness ranges between 0.4–0.8 μm and the N_t value ranges between $1 \times 10^{15} - 1 \times 10^{17}$ cm^{-3}, illustrated in Fig. 10b. Similarly, ETL PCBM exhibits the same result in Fig. 10c within the same range of absorber thickness and defect density (N_t).

Finally, the efficiency (PCE) is defined with variations in absorber thickness and defect density (N_t), shown in Fig. 11. According to Fig. 11a and d, the absorber thickness ranges from 0.4–0.8 μm and the N_t ranges from $1 \times 10^{15} -$ less than 1×10^{17} cm^{-3}, resulting in the maximum efficiency for WS_2 and TiO_2 being 19.70%. Fig. 11c displays an almost similar PCE of 19.60% for a PCBM-based optimized device when the absorber thickness is between 0.4–0.8 μm and N_t is between $1 \times 10^{15} -$ less than 1×10^{17} cm^{-3}. In contrast with the other ETLs in Fig. 11b, the ETL-based solar structure C_{60} exhibits lower PCE values, recording 18.70% at the same absorber thickness and defect density (N_t) ranges. For every device structure, the optimal thickness of ETLs is a crucial factor in achieving the highest possible PCE value.

3.5. Impact of absorber layer and HTL layer thickness of several ETLs on PV performance for $Cs_2CuBiBr_6$

3.5.1. Impact of absorber layer thickness. Perovskite solar cell's efficiency is greatly affected by the thickness of the absorber layer. This impact is significant because it enhances photon absorption, something that's vital for improving the device's general efficiency.[71] Given that the thickness of the absorber affects the performance of the ITO/ETL/$Cs_2CuBiBr_6$/CBTS/Ni structure, its value was increased from 0.4 to 1.2 μm to optimize the device. Fig. 12a illustrates the relationship between the PSC's performance and the change in the absorber thickness for each of the four distinct ETLs. Almost all designs showed a linear drop with increasing absorber thickness, and the greatest V_{OC} was approximately 0.73 V, demonstrating that they all performed similarly. The ITO/WS_2/$Cs_2CuBiBr_6$/CBTS/Ni PSC has the highest V_{OC} value (0.734 V) compared to other designs, whereas the ITO/PCBM/$Cs_2CuBiBr_6$/CBTS/Ni PSC has the lowest V_{OC} value (0.729 V). The WS_2, PCBM, and TiO_2 structures consistently increased with the absorber thickness for J_{SC}, with values varying from 33.43 to 37.24 mA cm^{-2} while the ITO/C_{60}/$Cs_2CuBiBr_6$/CBTS/Ni PSC exhibited a relatively lower value, ranging from 32.01 to
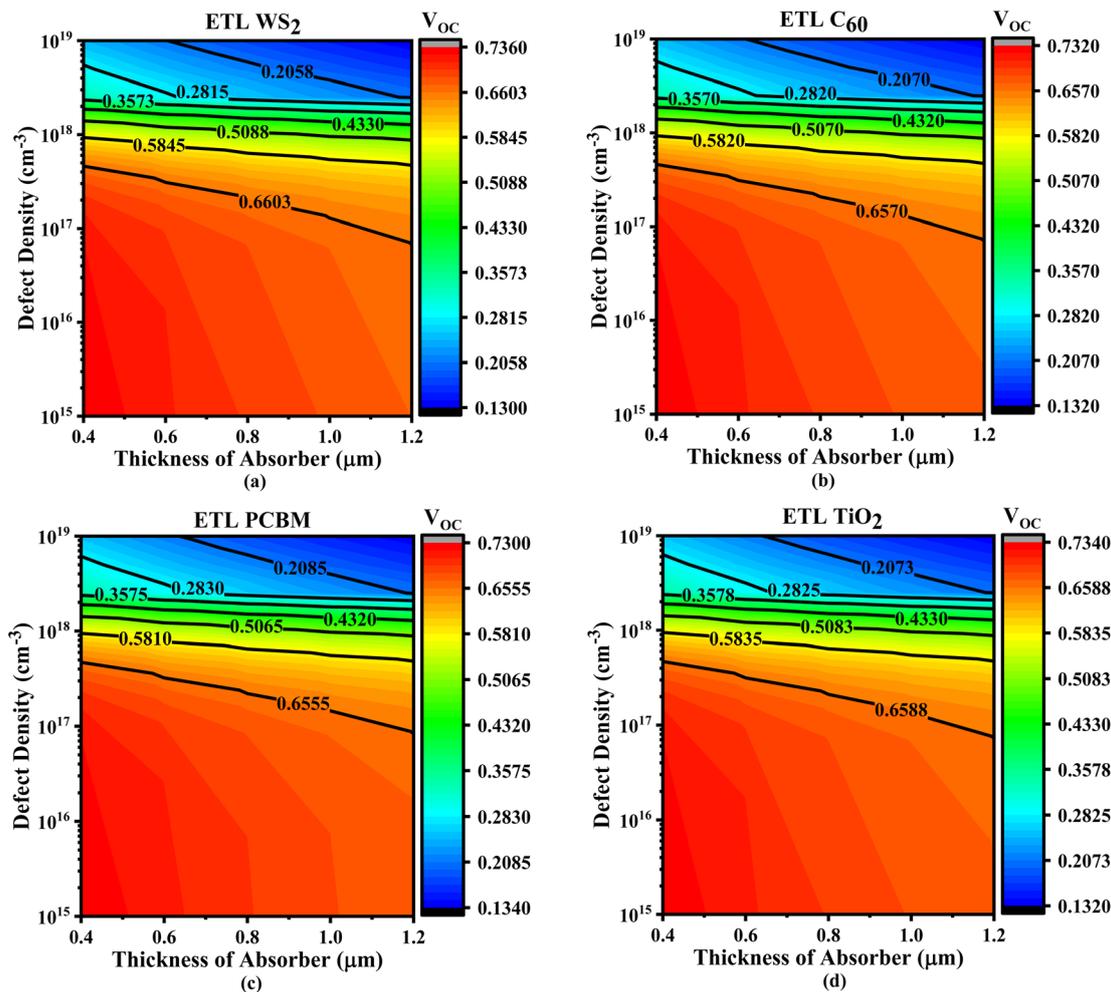
Fig. 8 Contour plots of V_{OC} resulting from the concurrent variation in defect density and absorber layer thickness with ETLs including (a) WS$_2$, (b) C$_{60}$, (c) PCBM, and (d) TiO$_2$.

35.64 mA cm^{-2}, despite displaying comparable characteristics. For ETL-based structures, the FF decreased linearly when the absorber layer thickness increased; the maximum FF was observed in WS$_2$, which ranged from 78.95% to 71.66%. TiO$_2$ and PCBM exhibited a similar trend, dropping from 78.91% to 71.31%, and C$_{60}$ stayed relatively constant between 78.65% and 71.54%. Regarding PCE, all configurations demonstrated an identical decreasing pattern with increased absorber thickness. When the thickness was 0.6 μm, the WS$_2$ ETL-based structure had a maximum efficiency of around 19.70%, but the C$_{60}$-based structure had the lowest efficiency rating, at about 18.69%. When investigating PCBM and TiO$_2$, it showed that the maximum efficiencies at 0.6 μm were 19.52% and 19.65%, respectively.

3.5.2. Impact of HTL layer thickness. Fig. 12b illustrates the effects of adjusting the thickness of a CBTS HTL with PV characteristics in Cs$_2$CuBiBr$_6$-based PSCs, using WS$_2$, C$_{60}$, PCBM, and TiO$_2$ as ETLs. Fig. 12b demonstrates that the V_{OC}, J_{SC}, FF, and PCE values for each ETL exhibit comparable patterns with increasing thickness. We only considered CBTS as the HTL in the thickness optimizations, as it was the only material that demonstrated the highest PCE. When the

thickness of CBTS increases, the V_{OC} value for WS$_2$, C$_{60}$, PCBM, and TiO$_2$ as ETLs stays the same at about 0.712 V, 0.709 V, 0.709 V, and 0.711 V. For J_{SC}, WS$_2$, PCBM, and TiO$_2$-based structures showed the highest and identical value of around 35.6 mA cm^{-2}, with the C$_{60}$-based structure exhibiting the lowest value of 34.07 mA cm^{-2} when the CBTS thickness increased. Considering a value of around 77.57% for the FF and 19.70% for the PCE, the WS$_2$-based ETL exhibits the maximum value. The PCBM ETL-based solar cell has the lowest FF value, measuring around 77.35%, while the C$_{60}$-based ETL has the lowest PCE value, measuring about 18.69%, as the CBTS thickness increases. Variation of thickness may have minimal impact if the HTL material has appropriate electrical conductivity and is aligned with the absorber and electrode's energy levels. The precise thickness of the HTL may not have a major impact on performances as long as it efficiently promotes hole transmission. The best possible thickness for greater PCE was found to be 0.1 μm, based on the variation in the HTL thickness. Consequently, 0.1 μm was determined to be the ideal HTL thickness for further analysis, which was also aligned with previous research.[72]
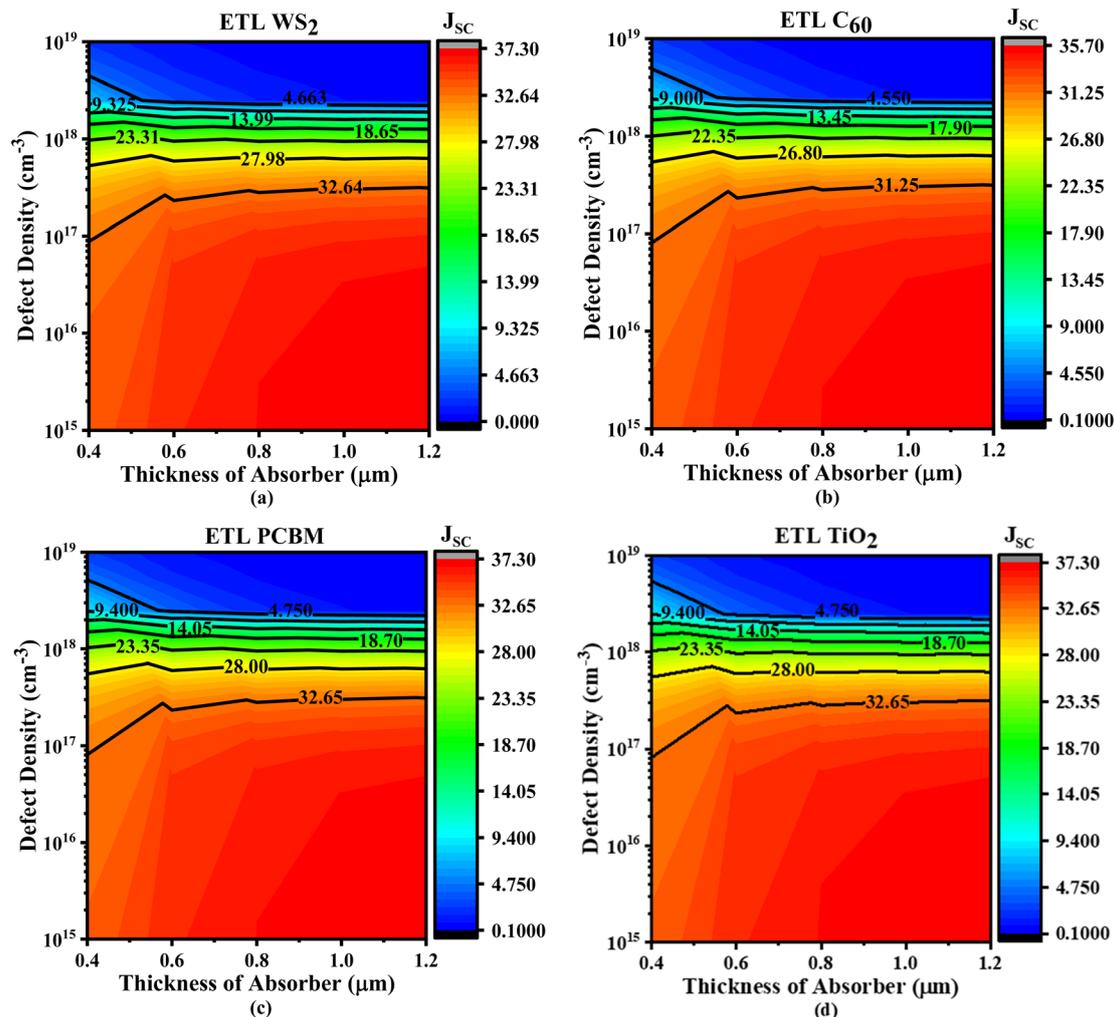
Fig. 9 Contour plots of J_{SC} resulting from the concurrent variation in defect density and absorber layer thickness with ETLs including (a) WS$_2$, (b) C$_{60}$, (c) PCBM, and (d) TiO$_2$.

3.6. Impact of series resistance, shunt resistance and temperature of several ETLs on PV performance for Cs$_2$CuBiBr$_6$

3.6.1. Impact of series resistance. Series (R_s) and shunt (R_{sh}) resistance have a major impact on SCs efficiency and are primarily caused by the relationships across the solar cell layers, the metal contacts on each side, and manufacturing defects.[51] While the effect of R_s ranged from 1 to 6 Ω cm^2, the shunt resistance was constant at 10^5 Ω cm^2 for the four individual perovskite devices, as shown in Fig. 13a. For every single structure of the Cs$_2$CuBiBr$_6$ perovskite device, the PCE dropped as the value of R_s changed. The PCE dropped from about 18.62% to 13.41% in devices that used WS$_2$, PCBM, and TiO$_2$-based Cs$_2$CuBiBr$_6$ perovskites. Concurrently, the PCE of the C$_{60}$-based Cs$_2$CuBiBr$_6$ perovskite device dropped from around 17.71% to 13.08% when the R_s increased. The FF of the ITO/WS$_2$/Cs$_2$CuBiBr$_6$/CBTS/Ni perovskite solar cells (PSCs) dropped from 73.3% to 53.35%. In contrast, the FF values of C$_{60}$ ETL decreased from 73.31% to 54.2% and PCBM-based structures decreased from 73.09% to 53.18%, correspondingly. On the

other hand, the FF value of TiO$_2$ ETL decreased from 73.25% to 53.29%. Regardless of changes in R_s, the J_{SC} value remained constant for WS$_2$, C$_{60}$, PCBM, and TiO$_2$ ETL-based structures. The constant values for WS$_2$, C$_{60}$, PCBM, and TiO$_2$ ETL-based structures are around 35.62, 34.06, 35.58, and 35.62 mA cm^{-2}, respectively. As the thickness of the CBTS increases, the V_{OC} value stays stable at approximately 0.712 V, 0.709 V, 0.707 V, and 0.711 V when using WS$_2$, C$_{60}$, PCBM, and TiO$_2$ as ETLs. Consequently, in PSCs and modules with large areas, several types of variables, including consistency, R_s and R_{sh} participate in a decrease with performance, especially within the FF.[73–75]

3.6.2. Impact of shunt resistance. An electrical element called the shunt resistance (R_{sh}) within the device affects the efficiency of solar cells. Any current that escapes from the active layer, the electrodes, or the region between donors and acceptors is a result of this resistance.[72] We observed the impact on the PV parameters for the ITO/ETL/Cs$_2$CuBiBr$_6$/CBTS/Ni heterostructure with varying R_{sh} from 10^1 to 10^6 Ω cm^2 and a constant R_s of 0.5 Ω cm^2 in Fig. 13b. A similar trend was observed in the V_{OC}, FF, and PCE values when R_{sh} increased. Regardless, for
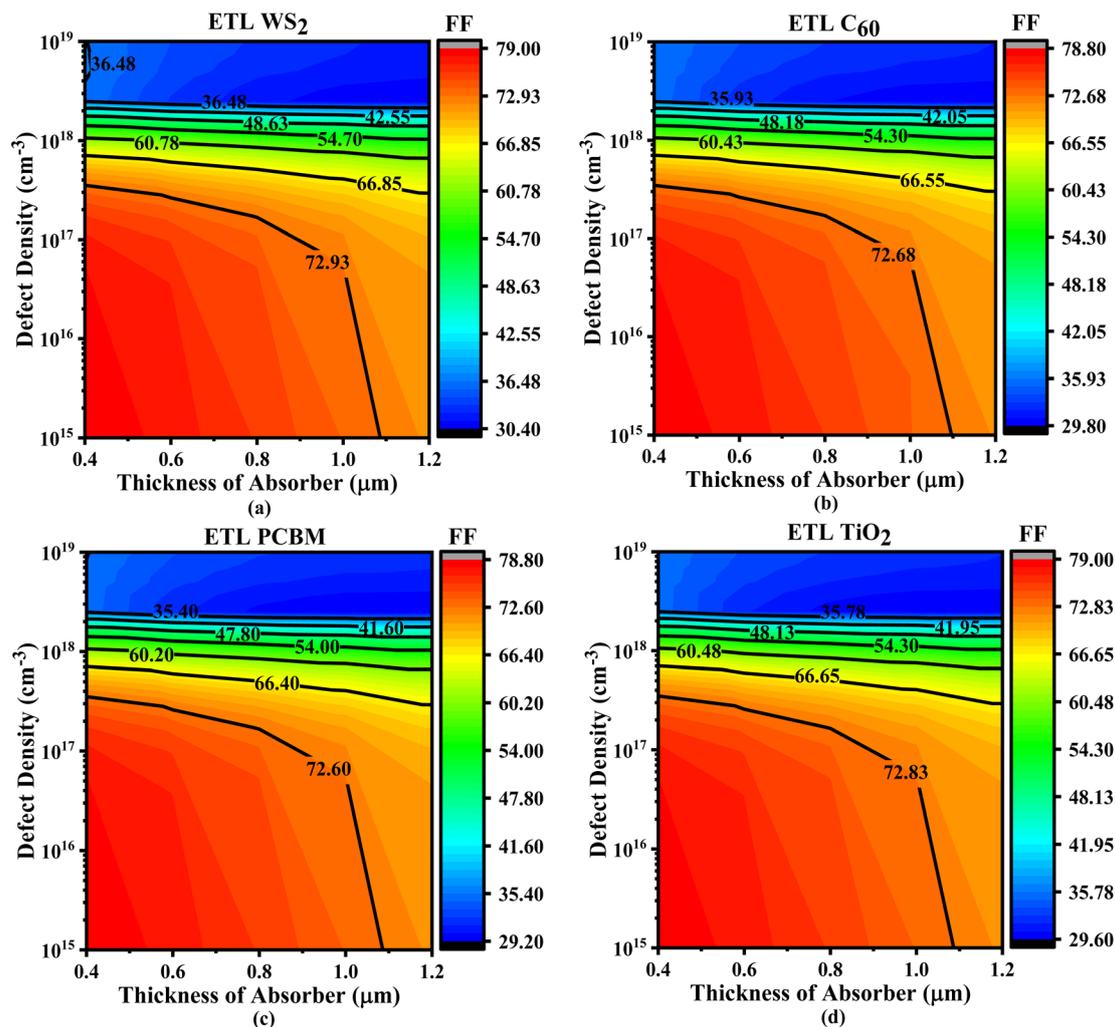
Fig. 10 Contour plots of FF resulting from the concurrent variation in defect density and absorber layer thickness with ETLs including (a) WS$_2$, (b) C$_{60}$, (c) PCBM, and (d) TiO$_2$.

each of the four structures, J_{SC} is constant. A sudden rise in the V_{OC}, FF, and PCE values was recorded between 10^1 to 10^2 Ω cm^2 of R_{sh} value. Following this increase, the PV parameters remained constant above a R_{sh} of 10^3 Ω cm^2. A possible explanation for this might be that, after a certain R_{sh} threshold is reached, the p–n junction provides a low-resistance route for the flow of junction current.[51] At R_{sh} value of $\approx 10^2$ Ω cm^2, the highest V_{OC} is 0.7 V, PCE is 19%, and FF is 77%. When R_{sh} changed, the J_{SC} values of the WS$_2$, C$_{60}$, PCBM, and TiO$_2$ ETL-based structures remained similar at 35.63, 34.07, 35.59, and 35.62 mA cm^{-2}, consequently. At 77.55%, the ITO/ETL/Cs$_2$-CuBiBr$_6$/CBTS/Ni PSC had the greatest FF of all the structures. The PCE value of 19.7% was the highest for the ITO/ETL/Cs$_2$-CuBiBr$_6$/CBTS/Ni PSC. For optimal device operation, it's necessary to set the series resistance to a minimum and the shunt resistance to a maximum value.[76]

3.6.3. Impact of temperature. Fig. 13c exhibits the effects of operating the device at temperatures ranging from 300 K to 450 K on its performance characteristics. Fig. 13c demonstrates the effects of varying temperatures on four distinct PSC structures.

As we varied the temperature, we observed changes in V_{OC}, J_{SC}, FF, and PCE across all four structures. Depicted in Fig. 13c, the values of PCE, FF, and V_{OC} decrease as the temperature increases for almost all structures of optimal solar cells. Conversely, J_{SC} stays approximately the same across all optimum device structures, regardless of temperature fluctuations. At a temperature of 300 K, the ITO/WS$_2$/Cs$_2$CuBiBr$_6$/CBTS/Ni PSC demonstrated the best efficiency, which was around 19.7%; however, the ITO/C$_{60}$/Cs$_2$CuBiBr$_6$/CBTS/Ni PSC attained the lowest efficiency, which was approximately 18.69%. During this study, the FF of the ITO/WS$_2$/Cs$_2$CuBiBr$_6$/CBTS/Ni PSC dropped from 77.55% to 60.1% as the temperature increased. Moreover, FF dropped for the remaining three PSCs when temperature rose. For all four structures, the J_{SC} of the PSCs under investigation did not fluctuate with increasing temperature. This indicates that temperature did not have any effect on the J_{SC}. There was a consistent pattern of decreasing V_{OC}s with increasing temperature across all four structures. For WS$_2$, the V_{OC} values were about 0.712 V, with the lowest at around 0.394 V. When temperatures rose, the reverse saturation
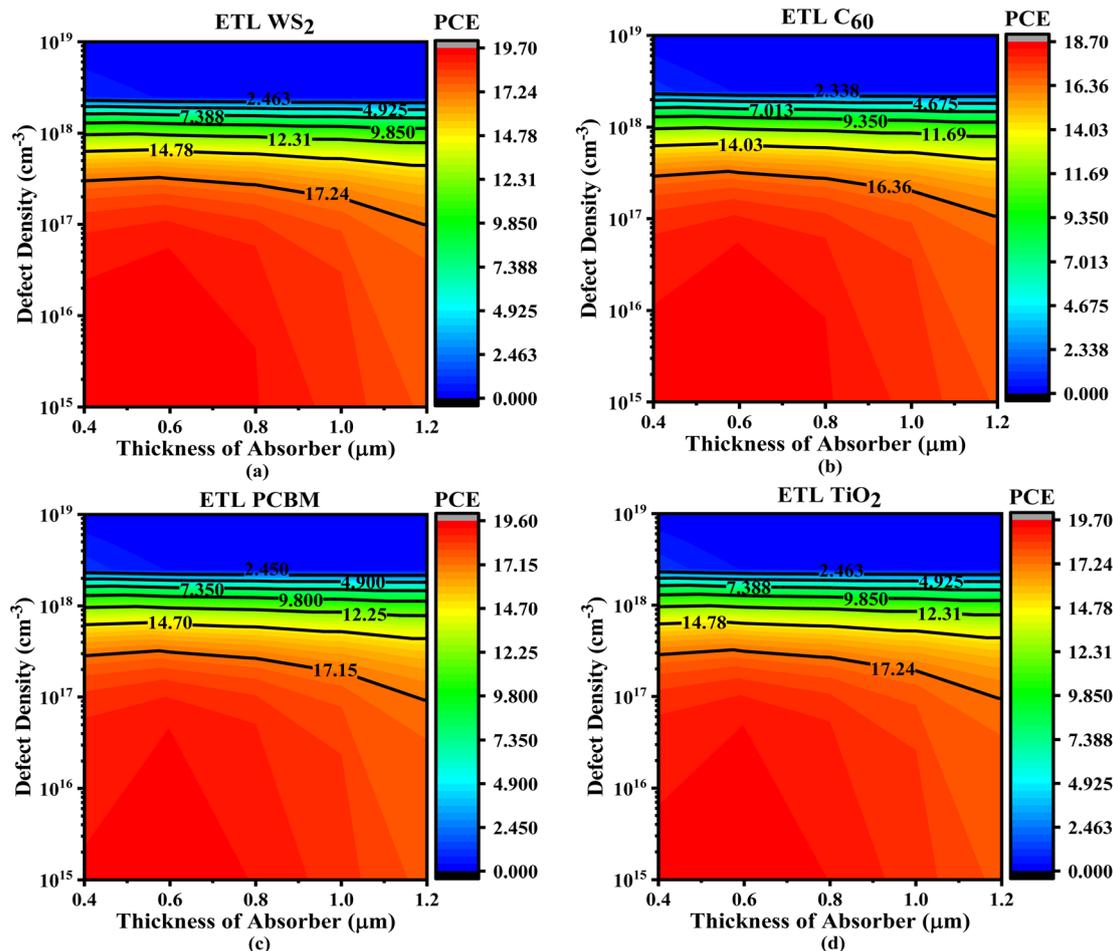
Fig. 11 Contour plots of PCE resulting from the concurrent variation in defect density and absorber layer thickness with ETLs including (a) WS₂, (b) C₆₀, (c) PCBM, and (d) TiO₂.

current density (J_0) increased, and as a result, the inverse relationship between V_{OC} and J_0 caused the V_{OC} values to drop across all ideal device structures. The interaction between V_{OC} and J_0 is seen in eqn (11).

$$V_{OC} = \frac{AK'T_1}{q}\left[\ln\left(1 + \frac{J_{SC}}{J_0}\right)\right] \tag{11}$$

Previous studies indicate that as the PSC temperature increases, the V_{OC} value decreases due to the presence of more defects.[51] The bandgap decreased with increasing temperature, which had little effect on the current. However, this alternation appears to remain stable as the temperature rises, despite its small size. The FF and PCE of the device are affected by changes in diffusion length and R_s, which happen as temperature increases.[77,78]

3.7. Effect of capacitance, Mott–Schottky, generation and recombination rate of several ETLs on PV performance for Cs₂CuBiBr₆

3.7.1. Effects of capacitance and Mott–Schottky (MS). Fig. 14a shows the capacitance (C) per unit area plot for four

solar cells with a bias voltage (V), and Fig. 14b shows the Mott–Schottky (M–S) plot. The charge carrier density (N_d) and built-in voltage (V_{bi}) can be determined by C–V measurements using the common M–S experimental method. It is used in typical P–N and semiconductor/metal junction devices with space charge regions and fixed depletion layers. The values of the junction capacitance per area (C) are given by eqn (12).

$$\frac{1}{C^2} = \frac{2\varepsilon_0\varepsilon_r}{qN_d}(V_{bi} - V) \tag{12}$$

According to Fig. 14b, the variables ε_r, q, V, and ε_0 stand for the donor's dielectric constant, electronic charge, applied voltage, and vacuum permittivity, respectively.[79] V_{bi} is produced by the prolongation of the linear component to the voltage axis, whereas N_d is produced by the gradient of the linear component. In both scenarios (Fig. 14a and b), the voltage varies between −0.8 to 0.8 V, and the frequency remains constant at 1 MHz. All enhanced devices exhibit an exponential rise in capacitance with increasing applied voltage, as shown in Fig. 14a. At 0.6 V, the solar structures based on WS₂, C₆₀, PCBM, and TiO₂ ETL exhibit an exponential rise. Particularly, the
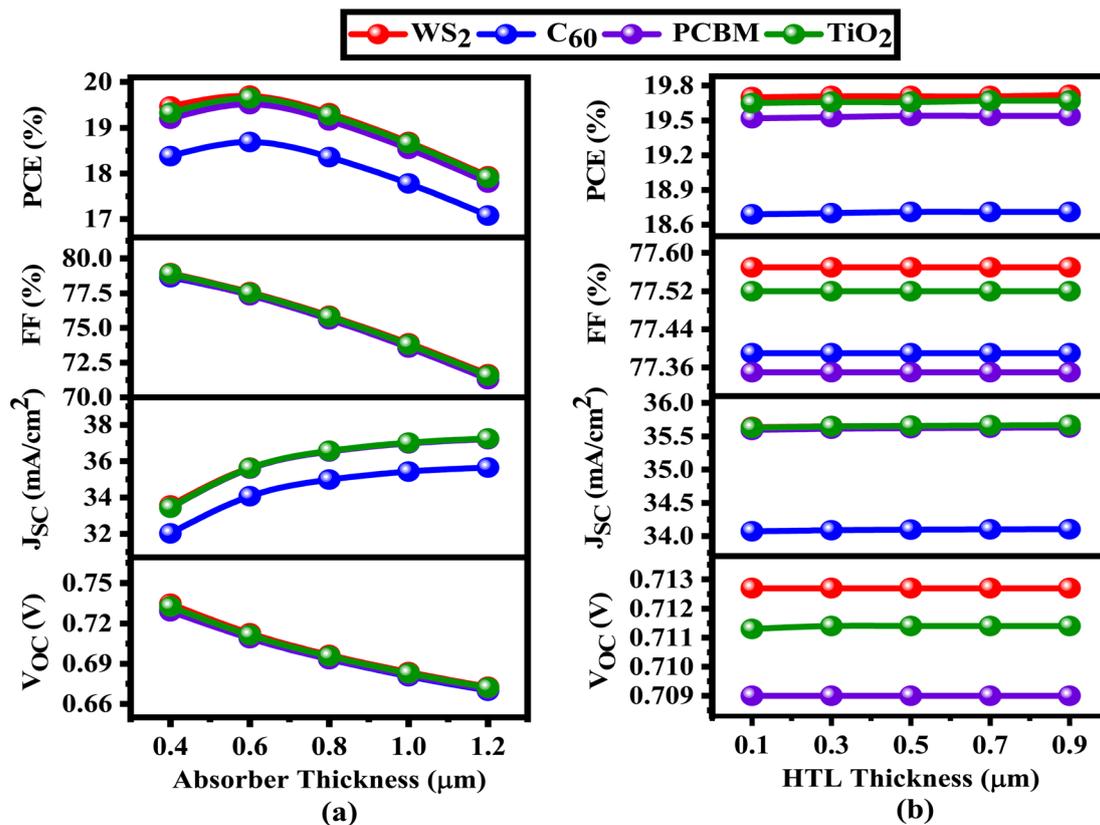
Fig. 12 Impact of photovoltaic (PV) variables (PCE, FF, J_{SC} and V_{OC}) given the modification in (a) absorber thickness and (b) HTL thickness of $Cs_2CuBiBr_6$.

PCBM-based ETL configuration has the greatest capacitance value, at about 710 nF cm^{-2}. The capacitance value of the C_{60}-based PSC is approximately 661 nF cm^{-2}, while the WS$_2$ and TiO$_2$ ETL-based PSCs have capacitance values of approximately 680 nF cm^{-2} and 693 nF cm^{-2}, respectively. Various ETL-associated solar configurations, as depicted in Fig. 14a, could represent the independent voltage capacitance resulting from the saturation of the depletion layer capacitance. Prior studies have shown that even at low voltages, the current remains substantially below saturation values, and that saturation occurs only at voltage peaks located at the points of contact.[80] This material has significant prospects as a voltage-controlled solar cell since its capacitance fluctuates as an effect of voltage.

Conversely, the built-in potential (V_{bi}), which is the difference between the electrode operation and doping level operations, may be effectively and widely determined with the M–S. The p–n junction is the main structure of the M–S theory, with the x-axis intercept usually referring to the V_{bi} of the semiconductor devices. Different electrode operation functions are used to find the slope of $1/C^2(V)$, which hows the percentage of engaged entrapment centers with lower values as expected.[81]

3.7.2. Effects of generation and recombination rate. The generation and recombination rates for four distinct structures are shown in Fig. 14c and d. When the electron moves from the valence band to the conduction band, it creates a hole in the valence band. This process occurs during generation, which

involves the production of electron–hole pairs.[68] Carrier generation is caused by the release of electrons and holes across the process. In all four configurations, Fig. 14c indicates the generation rates peak at around 0.7 µm for the TiO$_2$ structure. SCAPS-1D utilizes the incoming photon flux $N_{phot}(\lambda,x)$ to investigate the formation of electron–hole pairs $G(x)$. It is possible to determine the value of $G(x)$ by using eqn (13), which is derived from the photon flux for point and wavelength.

$$G(\lambda,x) = \alpha(\lambda,x)N_{phot}(\lambda,x) \qquad (13)$$

In contrast, the generation rate involves the creation of new electrons and holes in the conduction band, whereas the recombination rate involves their elimination. The lifetime and charge carrier density of a solar cell define its recombination rate. In the initial stages, the existence of defect states inside the absorber layer causes a decrease in the amount of electron–hole recombination. Consequently, the formation of energy levels impacts the electron–hole recombination rate inside the solar cell structure. In this case, WS$_2$ ETL-based PSCs have a maximum recombination rate of 0.303 µm, shown in Fig. 14d.

3.8. J–V and QE characteristics of $Cs_2CuBiBr_6$

With voltage ranging from 0 to 0.72 V, Fig. 15a depicts the fluctuating pattern of the J–V characteristics for the four solar cell structures in the investigation. The current density of the
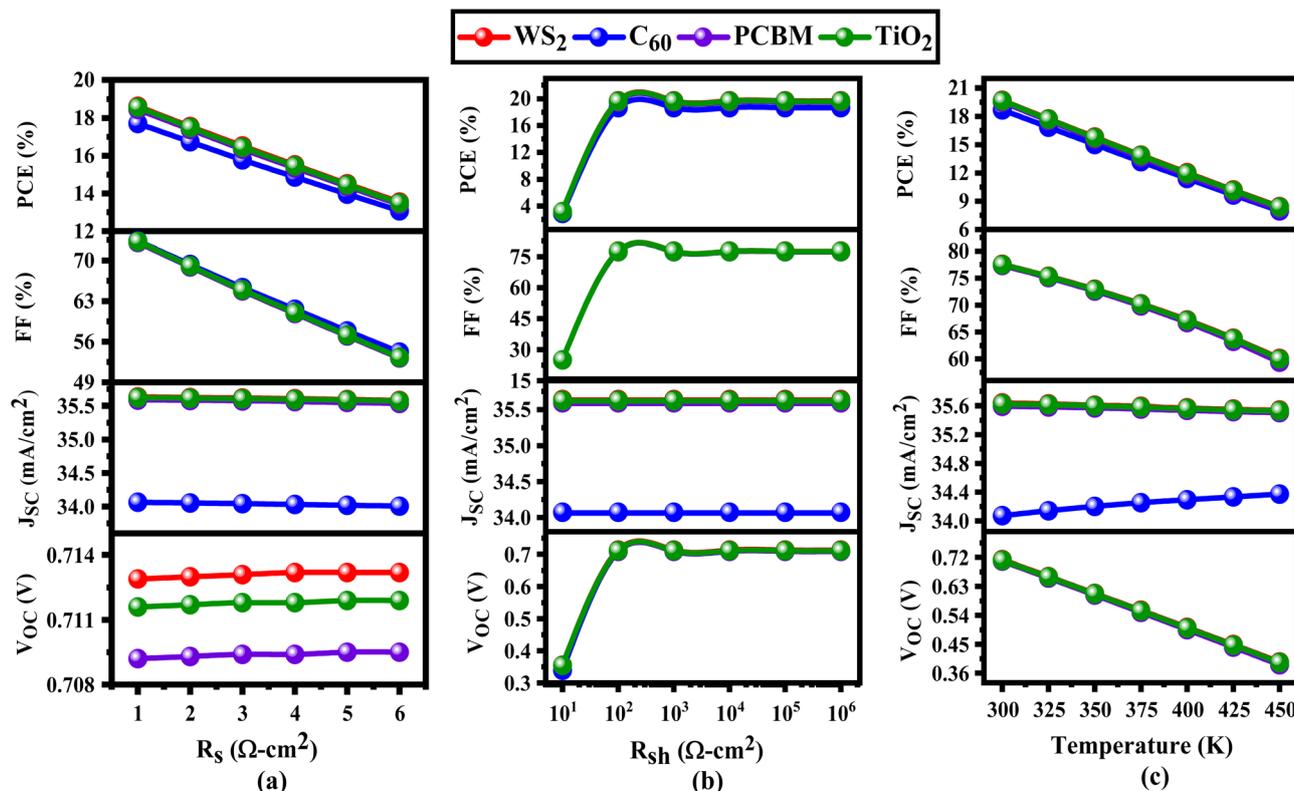
Fig. 13 Impact of photovoltaic (PV) variables (PCE, FF, J_{SC} and V_{OC}) given the modification in (a) series resistance (b) shunt resistance and (c) temperature of $Cs_2CuBiBr_6$.

C_{60}-associated PSC is roughly 34.07 mA cm^{-2}, as shown in Fig. 15a, while the J_{SC} of the PCBM-associated device is almost 35.59 mA cm^{-2}. The other two ETL-associated devices perform better than the C_{60} and PCBM-associated devices. In Fig. 15a, the ETL-associated structures of WS$_2$ and TiO$_2$ showed an open circuit voltage density of unity and a current density of 35.63 mA cm^{-2}. The device's efficiency is greatly affected by defects in perovskite films because photoelectrons are created inside these layers. The behavior of electron–hole recombination significantly influences the photovoltaic characteristics of the PSC. The interaction between the J–V curve and the bulk trap density is shown in Fig. 15a for a perovskite film. If defect states exist in perovskite films, there is a significant drop in all photovoltaic films. These findings are consistent with the assumption that perovskite solar structures with a high degree of crystallinity reduce charge recombination and improve performance.[82]

Fig. 15b exhibits the quantum efficiency (QE) graphs for all the devices associated with the research. In this case, the wavelength is changed from 300 to 1100 nm. The exponential increase is seen in Fig. 15b for all structures in the 300 to 360 nm range. The value is consistent across a wide range of around 360 to 600 nm. The QE of the PSCs according to the research at that time was determined to be unaffected by wavelength. Subsequently, the quantum efficiency declines across all structures as the wavelength increases. The QE for the ITO/C_{60}/$Cs_2CuBiBr_6$/CBTS/Ni PSC in Fig. 15b was slightly lower

than that of the other structures. In contrast, regarding wavelength variation, the other three PSCs showed approximately equivalent levels of efficiency. As the thickness of the absorber rises, the quantum efficiency (QE) also rises. This happens because a thicker absorber can absorb more photons.[83]

3.9. Results from SCAPS-1D are compared to earlier research

The performance characteristics of four device combinations with the recently published optimal configurations are compared in Table 4. Compared to the previously reported $Cs_2CuBiBr_6$ device structure, Table 4 demonstrates that the optimal $Cs_2CuBiBr_6$ double perovskite-based solar cell exhibits a higher PCE value. Four sets of device structures were presented with power conversion efficiencies (PCEs) of 19.70%, 18.69%, 19.52%, and 19.65%. In contrast, previously published device structures, such as the FTO/WS$_2$/$Cs_2CuBiBr_6$/spiro-OMeTAD/Ag configuration, show a considerably reduced efficiency of around 14.08%.[21] The exhibited solar structures have greater V_{OC} levels compared to the published configurations of devices. Conversely, the solar structure that has been given exhibits greater J_{SC} and FF values than the previously reported $Cs_2CuBiBr_6$-based device structure. All of the solar structures mentioned have V_{OC} values over 0.7 V and FF values above 77%, but the device structure that was previously published has the lowest V_{OC} and FF values. The four solar structures shown in Table 4 performed more effectively than the previously described $Cs_2CuBiBr_6$-based solar cells.

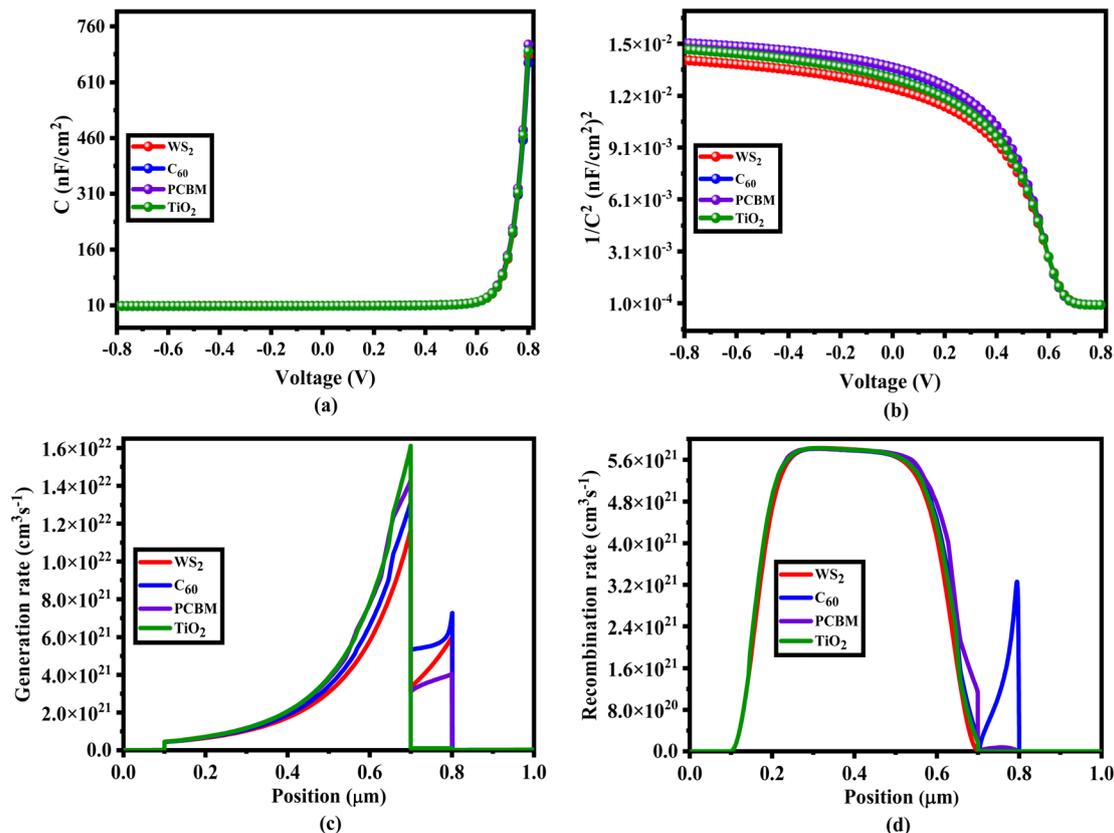**Fig. 14** Distinctions in (a) capacitance (b) Mott–Schottky (c) generation and (d) recombination of $Cs_2CuBiBr_6$.

The performance parameters of the four device configurations that were presented in Table 4 are compared to the optimum configurations that were recently published. In comparison to the previously reported $Cs_2B'B''Br_6$ device structure, Table 4 demonstrates that the optimal $Cs_2CuBiBr_6$ double perovskite-based solar cell exhibits a greater PCE value. In Table 4, the fifth solar cell device structure used spiro-OMeTAD HTL, resulting in 14.08% efficiency compared to our

present study of HTL CBTS. The emphasis of our investigation was on the properties of the absorber, such as its defect density, which were different from those of previous theoretical research on device structures. The characteristics of our study's ETL and HTL combinations also differed from those used in previous theoretical assessments. The optical characteristics of the absorber also influence the absorption of solar energy. By achieving 14.08% PCE in the FTO/WS₂/Cs₂CuBiBr₆/spiro-
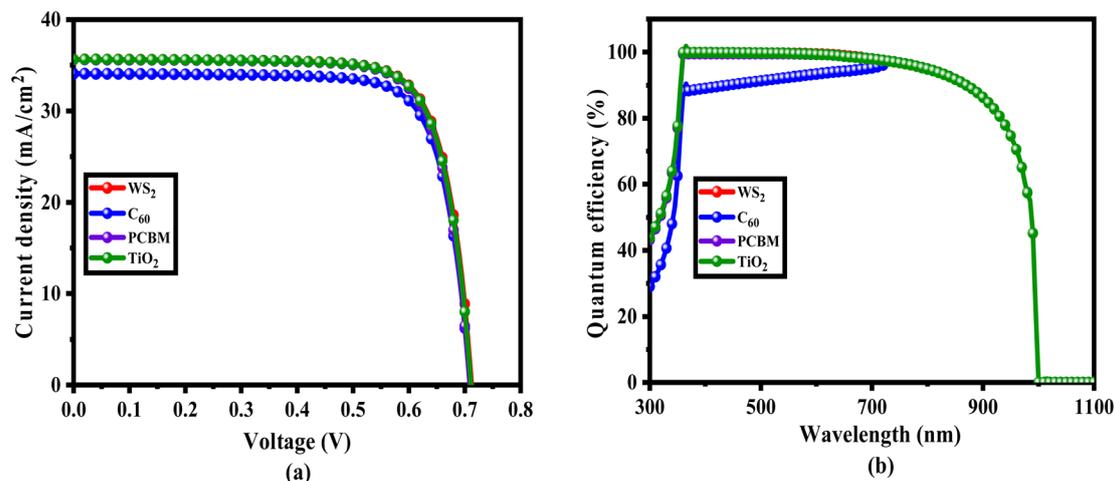

Fig. 15 Optimization of the (a) J–V characteristic curve and (b) the quantum energy curve of $Cs_2CuBiBr_6$.

Table 4 The comparison of PV parameters of $Cs_2CuBiBr_6$ and similar absorbers-based SCs[a]

Type	Optimized devices	V_{OC} (V)	J_{SC} (mA cm^{-2})	FF (%)	PCE (%)	Ref.
E	FTO/TiO$_2$/Cs$_2$AgBiBr$_6$/spiro-OMeTAD/MoO$_3$/Ag	1.01	3.82	65	2.51	84
E	FTO/c-TiO$_2$/mTiO$_2$/Cs$_2$AgBiBr$_6$/N719/spiro-OmeTAD/Ag	1.06	5.13	—	2.84	85
E	FTO/TiO$_2$/Cs$_2$AgBiBr$_6$/spiro-OMeTAD/Au	1.511	3.89	51.76	3.04	86
T	ITO/SnO$_2$/Cs$_2$AgBiBr$_6$/spiro-OMeTAD/Au	0.92	11.4	60.93	6.37	87
T	FTO/WS$_2$/Cs$_2$CuBiBr$_6$/spiro-OMeTAD/Ag	0.60	34.59	67.36	14.08	21
T	FTO/TiO$_2$/Cs$_2$AgSbBr$_6$/spiro-OMeTAD/Ag	0.94	22.49	50.2	10.69	21
T	ITO/WS$_2$/Cs$_2$CuBiBr$_6$/CBTS/Ni	0.712	35.63	77.57	19.70	This work
T	ITO/C$_{60}$/Cs$_2$CuBiBr$_6$/CBTS/Ni	0.709	34.07	77.39	18.69	This work
T	ITO/PCBM/Cs$_2$CuBiBr$_6$/CBTS/Ni	0.709	35.59	77.35	19.52	This work
T	ITO/TiO$_2$/Cs$_2$CuBiBr$_6$/CBTS/Ni	0.711	35.62	77.52	19.65	This work

[a] E – experimental, T – theoretical.

OMeTAD/Ag structure, the improved optical characteristics of the $Cs_2CuBiBr_6$ absorber were observed.[21] The above justifies the conclusion that, compared with previously researched Cs_2-$CuBiBr_6$-based, differently structured solar cells, our Cs_2-$CuBiBr_6$ solar cell exhibits superior PCE.

4. Conclusion

The research objective is to investigate the SCAPS-1D simulation results and determine the possibility of developing perovskites based on cesium copper bismuth bromide. The four solar designs (ITO/WS$_2$/Cs$_2$CuBiBr$_6$/CBTS/Ni, ITO/C$_{60}$/Cs$_2$CuBiBr$_6$/CBTS/Ni, ITO/PCBM/Cs$_2$CuBiBr$_6$/CBTS/Ni, ITO/TiO$_2$/Cs$_2$CuBiBr$_6$/CBTS/Ni) are compared in terms of their PV properties. Among all the investigated structures, ITO/WS$_2$/Cs$_2$CuBiBr$_6$/CBTS/Ni demonstrated the greatest performance with PCE of 19.70%, V_{OC} of 0.712 V, J_{SC} of 35.63 mA cm^{-2}, and FF of 77.57%. An advantageous band alignment is responsible for this higher performance. The absorber layer falls within the range of 0.4 to 1.2 μm, with the highest efficiency occurring at 0.6 μm. The thickness of the electron transport layers (ETLs) varies between 0.03 and 0.15 μm for the four different perovskite solar cell structures. Device efficiency is further improved by optimizing the HTL thickness between 0.1 and 0.5 μm. PV characteristics are greatly impacted by changes in defect density (N_t), whereas PCE and FF are adversely affected by series resistance without significantly impacting J_{SC} and V_{OC}. While V_{OC}, FF, and PCE increase with shunt resistance, enhancing at 10^2 Ω cm^2, the J_{SC} stays constant. From 300 to 450 K, the performance of WS$_2$-based ETL structures remains preferable; as the temperature rises, PCE, V_{OC}, and FF drop but J_{SC} stays constant. In particular, at around 710 nF cm^{-2}, the PCBM-based ETL structure has the highest capacitance value. When the rates of generation and recombination were investigated, the ITO/WS$_2$/Cs$_2$CuBiBr$_6$/CBTS/Ni structures exhibited the maximum recombination at 0.303 μm and the ITO/TiO$_2$/Cs$_2$CuBiBr$_6$/CBTS/Ni configurations showed the most generation at 0.7 μm. J–V characteristics and quantum efficiency (QE) analysis both demonstrated superior performance WS$_2$ ETL devices. For the development of double perovskite-based innovations, these outcomes provide significant information for improving solar cell designs.

Data availability

Data will be made available on request.

Author contributions

Khandoker Isfaque Ferdous Utsho: investigation, methodology, data curation, conceptualization, writing original manuscript; S. M. G. Mostafa: investigation, methodology, data curation, review-editing; Md. Tarekuzzaman: formal analysis, software, conceptualization, review-editing; Muneera S. M. Al-Saleem: formal analysis, methodology, data curation, review-editing; Nazmul Islam Nahid: formal analysis, methodology, data curation, review-editing; Jehan Y. Al-Humaidi: formal analysis, methodology, data curation, review-editing; Md. Rasheduzzaman: formal analysis, validation, review-editing; Mohammed M. Rahman: formal analysis, validation, supervision, review-editing; Md. Zahid Hasan: formal analysis, validation, supervision, review-editing.

Conflicts of interest

There is no conflict to declare.

Acknowledgements

References

1 M. Hosenuzzaman, N. A. Rahim, J. Selvaraj, M. Hasanuzzaman, A. A. Malek and A. Nahar, *Renewable Sustainable Energy Rev.*, 2015, **41**, 284–297.

2 K. Ranabhat, L. Patrikeev, A. A. Revina, K. Andrianov, V. Lapshinsky and E. Sofronova, *J. Appl. Eng. Sci.*, 2016, **31**, 103532.

3 S. B. Verma, *Emerging Trends in IoT and Computing Technologies*, 2022.

4 J. N. Davis, Master's thesis, The University of Utah, 2023.

5 A. M. Bagher, M. Vahid and M. Mohsen, *Int. J. Renewable Sustainable Energy*, 2014, **3**, 59–67.

6 H. Al Dmour, *East Eur. J. Phys.*, 2023, **3**, 555–561.

7 H. Al-Dmour, D. M. Taylor and J. A. Cambridge, *J. Phys. D:Appl. Phys.*, 2007, **40**, 5034.

8 M. T. Kibria, A. Ahammed, S. M. Sony, F. Hossain and S. U. Islam, in *Proc. of 5th*, 2014, pp. 51–53.

9 K. K. Sharma, D. I. Patel and R. Jain, *Chem. Commun.*, 2015, **51**, 15129–15132.

10 H. Al-Dmour and D. M. Taylor, *Thin Solid Films*, 2011, **519**, 8135–8138.

11 A. Slami, M. Bouchaour and L. Merad, *Int. J. Energy Environ.*, 2019, **13**, 17–21.

12 S. Karthick, S. Velumani and J. Bouclé, *Sol. Energy*, 2020, **205**, 349–357.

13 A. Aftab and M. I. Ahmad, *Sol. Energy*, 2021, **216**, 26–47.

14 F. Baig, Y. H. Khattak, B. Marí, S. Beg, A. Ahmed and K. Khan, *J. Electron. Mater.*, 2018, **47**, 5275–5282.

15 H. Al-Dmour, R. H. Alzard, H. Alblooshi, K. Alhosani, S. AlMadhoob and N. Saleh, *Front. Chem.*, 2019, **7**, 561.

16 A. K. Mishra and R. K. Shukla, *SN Appl. Sci.*, 2020, **2**, 321.

17 H. Al-Dmour, S. Al-Trawneh and S. Al-Taweel, *Int. J. Adv. Appl. Sci.*, 2021, **8**, 128–135.

18 H. Kolya and C.-W. Kang, *Polymers*, 2023, **15**, 3421.

19 S. Shahi, PhD thesis, State University of New York at Buffalo, 2022.

20 H. Al-Dmour and D. M. Taylor, *J. Ovonic Res.*, 2023, **19**(5), 587–596.

21 R. Yao, S. Ji, T. Zhou, C. Quan, W. Liu and X. Li, *Phys. Chem. Chem. Phys.*, 2024, **26**, 5253–5261.

22 Z.-L. Huang, C.-M. Chen, Z.-K. Lin and S.-H. Yang, *Superlattices Microstruct.*, 2017, **102**, 94–102.

23 W. S. Yang, J. H. Noh, N. J. Jeon, Y. C. Kim, S. Ryu, J. Seo and S. I. Seok, *Science*, 2015, **348**, 1234–1237.

24 E. T. McClure, M. R. Ball, W. Windl and P. M. Woodward, *Chem. Mater.*, 2016, **28**, 1348–1354.

25 G. Volonakis, M. R. Filip, A. A. Haghighirad, N. Sakai, B. Wenger, H. J. Snaith and F. Giustino, *J. Phys. Chem. Lett.*, 2016, **7**, 1254–1259.

26 F. Igbari, Z. Wang and L. Liao, *Adv. Energy Mater.*, 2019, **9**, 1803150.

27 X.-G. Zhao, D. Yang, J.-C. Ren, Y. Sun, Z. Xiao and L. Zhang, *Joule*, 2018, **2**, 1662–1673.

28 H. Absike, N. Baaalla, R. Lamouri, H. Labrim and H. Ez-zahraouy, *Int. J. Energy Res.*, 2022, **46**, 11053–11064.

29 H. Wu, A. Erbing, M. B. Johansson, J. Wang, C. Kamal, M. Odelius and E. M. J. Johansson, *ChemSusChem*, 2021, **14**, 4507–4515.

30 H.-J. Feng, W. Deng, K. Yang, J. Huang and X. C. Zeng, *J. Phys. Chem. C*, 2017, **121**, 4471–4480.

31 J. Burschka, N. Pellet, S.-J. Moon, R. Humphry-Baker, P. Gao, M. K. Nazeeruddin and M. Grätzel, *Nature*, 2013, **499**, 316–319.

32 H. Bencherif and M. K. Hossain, *Sol. Energy*, 2022, **248**, 137–148.

33 Y.-F. Chiang, J.-Y. Jeng, M.-H. Lee, S.-R. Peng, P. Chen, T.-F. Guo, T.-C. Wen, Y.-J. Hsu and C.-M. Hsu, *Phys. Chem. Chem. Phys.*, 2014, **16**, 6033–6040.

34 S. Ryu, J. H. Noh, N. J. Jeon, Y. C. Kim, W. S. Yang, J. Seo and S. I. Seok, *Energy Environ. Sci.*, 2014, **7**, 2614–2618.

35 V. Sebastian and J. Kurian, *Sol. Energy*, 2021, **221**, 99–108.

36 H. Bencherif, L. Dehimi, N. Mahsar, E. Kouriche and F. Pezzimenti, *Mater. Sci. Eng., B*, 2022, **276**, 115574.

37 M. Khaouani, A. Hamdoune, H. Bencherif, Z. Kourdi and L. Dehimi, *Optik*, 2020, **217**, 164797.

38 F. Kherrat, L. Dehimi, H. Bencherif, M. M. A. Moon, M. K. Hossain, N. A. Sonmez, T. Ataser, Z. Messai and S. Özçelik, *Micro Nanostruct.*, 2023, **183**, 207676.

39 S. Chen, Y. Pan, D. Wang and H. Deng, *J. Electron. Mater.*, 2020, **49**, 7363–7369.

40 Y. Pan and W. Guan, *J. Power Sources*, 2016, **325**, 246–251.

41 J. Zhou, J. Hou, X. Tao, X. Meng and S. Yang, *J. Mater. Chem. A*, 2019, **7**, 7710–7716.

42 X. Guo, H. Dong, W. Li, N. Li and L. Wang, *ChemPhysChem*, 2015, **16**, 1727–1732.

43 B. Zaidi, N. Mekhaznia, M. S. Ullah and H. Al-Dmour, *J. Phys.: Conf. Ser.*, 2024, **2843**, 012012.

44 N. L. Dey, Md. S. Reza, A. Ghosh, H. Al-Dmour, M. Moumita, Md. S. Reza, S. Sultana, A. K. M. Yahia, M. Shahjalal, N. S. Awwad and H. A. Ibrahium, *J. Phys. Chem. Solids*, 2025, **196**, 112386.

45 X. Shi, Y. Ding, S. Zhou, B. Zhang, M. Cai, J. Yao, L. Hu, J. Wu, S. Dai and M. K. Nazeeruddin, *Adv. Sci.*, 2019, **6**, 1901213.

46 L. Cojocaru, S. Uchida, Y. Sanehira, J. Nakazaki, T. Kubo and H. Segawa, *Chem. Lett.*, 2015, **44**, 674–676.

47 K. Wang, Z. Jin, L. Liang, H. Bian, D. Bai, H. Wang, J. Zhang, Q. Wang and S. Liu, *Nat. Commun.*, 2018, **9**, 4544.

48 Y. H. Khattak, F. Baig, H. Toura, S. Beg and B. M. Soucase, *J. Electron. Mater.*, 2019, **48**, 5723–5733.

49 D. Shin, B. Saparov, T. Zhu, W. P. Huhn, V. Blum and D. B. Mitzi, *Chem. Mater.*, 2016, **28**, 4771–4780.

50 R. Chakraborty, K. M. Sim, M. Shrivastava, K. V. Adarsh, D. S. Chung and A. Nag, *ACS Appl. Energy Mater.*, 2019, **2**, 3049–3055.

51 M. K. Hossain, M. H. K. Rubel, G. F. I. Toki, I. Alam, Md. F. Rahman and H. Bencherif, *ACS Omega*, 2022, **7**, 43210–43230.

52 M. H. Ali, A. S. Islam, M. D. Haque, M. F. Rahman, M. K. Hossain, N. Sultana and A. T. Islam, *Mater. Today Commun.*, 2023, **34**, 105387.

53 R. Pandey, S. Bhattarai, K. Sharma, J. Madan, A. K. Al-Mousoi, M. K. A. Mohammed and M. K. Hossain, *ACS Appl. Electron. Mater.*, 2023, **5**, 5303–5315.

54 A. K Al-Mousoi, M. K. A. Mohammed, S. Q. Salih, R. Pandey, J. Madan, D. Dastan, E. Akman, A. A. Alsewari and Z. M. Yaseen, *Energy Fuels*, 2022, **36**, 14403–14410.

55 A. K. Al-Mousoi, M. K. Mohammed, R. Pandey, J. Madan, D. Dastan, G. Ravi and P. Sakthivel, *RSC Adv.*, 2022, **12**, 32365–32373.

56 R. A. Jabr, M. Hamad and Y. M. Mohanna, *Int. J. Electr. Eng. Educ.*, 2007, **44**, 23–33.

57 Y. H. Khattak, PhD thesis, Universitat Politècnica de València, 2019.

58 F. Anwar, S. Afrin, S. Satter, R. Mahbub and S. M. Ullah, *Int. J. Renew. Energy Res.*, 2017, **7**, 885–893.

59 Y. Gan, X. Bi, Y. Liu, B. Qin, Q. Li, Q. Jiang and P. Mo, *Energies*, 2020, **13**, 5907.

60 Y. Raoui, H. Ez-Zahraouy, N. Tahiri, O. El Bounagui, S. Ahmad and S. Kazim, *Sol. Energy*, 2019, **193**, 948–955.

61 K. Sekar, L. Marasamy, S. Mayarambakam, H. Hawashin, M. Nour and J. Bouclé, *RSC Adv.*, 2023, **13**, 25483–25496.

62 T. Minemoto and M. Murata, *Sol. Energy Mater. Sol. Cells*, 2015, **133**, 8–14.

63 H. Abnavi, D. K. Maram and A. Abnavi, *Opt. Mater.*, 2021, **118**, 111258.

64 D. K. Maram, M. Haghighi, O. Shekoofa, H. Habibiyan and H. Ghafoorifard, *Sol. Energy*, 2021, **213**, 1–12.

65 O. Gunawan, T. K. Todorov and D. B. Mitzi, *Appl. Phys. Lett.*, 2010, **97**, 233506.

66 C. Yan, F. Liu, N. Song, B. K. Ng, J. A. Stride, A. Tadich and X. Hao, *Appl. Phys. Lett.*, 2014, **104**, 173901.

67 S. Rai, B. K. Pandey and D. K. Dwivedi, *Opt. Mater.*, 2020, **100**, 109631.

68 M. K. Hossain, A. A. Arnab, R. C. Das, K. M. Hossain, M. H. K. Rubel, M. F. Rahman, H. Bencherif, M. E. Emetere, M. K. Mohammed and R. Pandey, *RSC Adv.*, 2022, **12**, 35002–35025.

69 S. Abdelaziz, A. Zekry, A. Shaker and M. Abouelatta, *Opt. Mater.*, 2020, **101**, 109738.

70 J. A. Owolabi, M. Y. Onimisi, J. A. Ukwenya, A. B. Bature and U. R. Ushiekpan, *Am. J. Phys. Appl.*, 2020, **8**, 8–18.

71 U. Mandadapu, S. V. Vedanayakam and K. Thyagarajan, *Indian J. Sci. Technol.*, 2017, **10**, 65–72.

72 M. K. Hossain, D. P. Samajdar, R. C. Das, A. A. Arnab, Md. F. Rahman, M. H. K. Rubel, Md. R. Islam, H. Bencherif, R. Pandey, J. Madan and M. K. A. Mohammed, *Energy Fuels*, 2023, **37**, 3957–3979.

73 E. Bi, W. Tang, H. Chen, Y. Wang, J. Barbaud, T. Wu, W. Kong, P. Tu, H. Zhu and X. Zeng, *Joule*, 2019, **3**, 2748–2760.

74 E. H. Jung, N. J. Jeon, E. Y. Park, C. S. Moon, T. J. Shin, T.-Y. Yang, J. H. Noh and J. Seo, *Nature*, 2019, **567**, 511–515.

75 D. Bogachuk, R. Tsuji, D. Martineau, S. Narbey, J. P. Herterich, L. Wagner, K. Suginuma, S. Ito and A. Hinsch, *Carbon*, 2021, **178**, 10–18.

76 A. Sunny, S. Rahman, M. Khatun and S. R. A. Ahmed, *AIP Adv.*, 2021, **11**, 065102.

77 S. R. Raga, E. M. Barea and F. Fabregat-Santiago, *J. Phys. Chem. Lett.*, 2012, **3**, 1629–1634.

78 F. Behrouznejad, S. Shahbazi, N. Taghavinia, H.-P. Wu and E. W.-G. Diau, *J. Mater. Chem. A*, 2016, **4**, 13488–13498.

79 S. Lin, Computer Solutions of the Traveling Salesman Problem, *Bell Syst. Tech. J.*, 1965, **44**, 2245–2269.

80 G. G. Malliaras, J. R. Salem, P. J. Brock and C. Scott, *Phys. Rev. B:Condens. Matter Mater. Phys.*, 1998, **58**, R13411–R13414.

81 M. Samiul Islam, K. Sobayel, A. Al-Kahtani, M. A. Islam, G. Muhammad, N. Amin, M. Shahiduzzaman and M. Akhtaruzzaman, *Nanomaterials*, 2021, **11**, 1218.

82 M. Liu, M. B. Johnston and H. J. Snaith, *Nature*, 2013, **501**, 395–398.

83 K. K. Maurya and V. N. Singh, *J. Sci.:Adv. Mater. Devices*, 2022, **7**, 100445.

84 F. Igbari, R. Wang, Z.-K. Wang, X.-J. Ma, Q. Wang, K.-L. Wang, Y. Zhang, L.-S. Liao and Y. Yang, *Nano Lett.*, 2019, **19**, 2066–2073.

85 X. Yang, Y. Chen, P. Liu, H. Xiang, W. Wang, R. Ran, W. Zhou and Z. Shao, *Adv. Funct. Mater.*, 2020, **30**, 2001557.

86 E. Greul, M. L. Petrus, A. Binek, P. Docampo and T. Bein, *J. Mater. Chem. A*, 2017, **5**, 19972–19981.

87 Z. Zhang, Q. Sun, Y. Lu, F. Lu, X. Mu, S.-H. Wei and M. Sui, *Nat. Commun.*, 2022, **13**, 3397.

© 2025 The Author(s). Published by the Royal Society of Chemistry